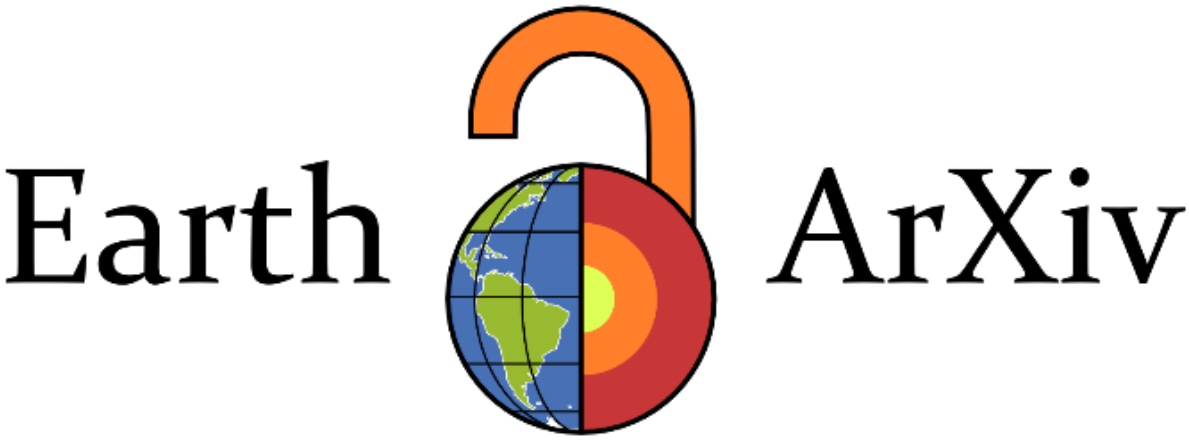

Paleobathymetric trends in Northern Hemisphere calcareous nannoplankton "boom-bust" successions following the Cretaceous/Paleogene (K/Pg) mass extinction

Heather L. Jones[1], Lorna E. Kearns[2], Julio Sepúlveda[3], Christopher M. Lowery[2], Laia Alegret[4], Thomas Westerhold[1], M. Hedi Negra[5], Michael Henehan[6], Jessica H. Whiteside[7], Johan Vellekoop,[8,9], Mark E. Patzkowsky[10] and Timothy J. Bralower[10]

Corresponding author contact: hjones@marum.de

1. MARUM – Center for Marine Environmental Sciences, University of Bremen, Germany.
2. Institute for Geophysics, Jackson School of Geosciences, University of Texas at Austin, USA.
3. Department of Geological Sciences and Institute of Arctic and Alpine Research (INSTAAR), University of Colorado Boulder, USA.
4. Departamento de Ciencias de la Tierra & Instituto Universitario de Ciencias Ambientales, Universidad Zaragoza, Spain.
5. Faculty of Sciences of Tunis, University of Tunis El Manar, Tunisia.
6. School of Earth Sciences, University of Bristol, UK.
7. Department of Earth & Environmental Sciences, San Diego State University, USA.
8. Department of Earth and Environmental Sciences, KU Leuven, Belgium
9. OD Earth and History of Life, Institute of Natural Sciences, Belgium
10. Department of Geosciences, Pennsylvania State University, USA.

Abstract

The Cretaceous/Paleogene (K/Pg) bolide impact ~66 Ma caused the near-demise of calcareous nannoplankton – key primary producers and major components of the biological pump that exports organic and inorganic carbon to the deep sea. Despite their ecological significance, resolving the exact impact of nannoplankton's mass extinction on ecosystem structure and function is complicated by marked global heterogeneity in paleoecological and biogeochemical responses. To explore this further, we generated a ~3.7 Myr nannofossil record from sediment cores at the Global Stratotype Section and Point for the basal Danian near El Kef, Tunisia, representing an outer continental shelf setting in the peri-Tethys Ocean. Our data reveal a series of low-diversity, high-abundance assemblages that persisted throughout the study interval. Although such boom-bust successions typify Northern Hemisphere nannoplankton recovery, statistical comparison with published datasets indicates that their duration – and the sequence of taxa comprising them – were location-specific and predominantly controlled by paleobathymetry, namely a site's position along a shelf-to-open-ocean transect. We hypothesize that this spatial variability reflects faster restoration of biological pump efficiency in open-ocean versus continental shelf settings, which in turn led to a quicker reduction in surface ocean nutrient availability. This would have encouraged the earlier proliferation of specialist, low-nutrient-adapted nannoplankton taxa with larger average cell volumes in open-ocean environments, further boosting pump efficiency via organic matter ballasting. Therefore, future research should prioritize disentangling the causal relationships between carbon cycling and nannoplankton recovery following the K/Pg extinction through rigorous integration of high-resolution biogeochemical time series and abundance-weighted nannofossil cell-volume data.

Plain Language Summary

The mass extinction that killed the dinosaurs ~66 million years ago also nearly wiped out calcareous nannoplankton, tiny algae that live in the surface ocean. These organisms are vital because they

support marine food webs and help transport carbon to the deep sea when their shells sink. Understanding how nannoplankton recovered after the extinction is challenging because species appeared and disappeared at different times across regions, and the marine carbon cycle recovered unevenly. To investigate this, we studied nannofossils from sediments spanning ~3.7 million years after the extinction at El Kef, Tunisia, which preserve an exceptional recovery record. We identified four recovery phases, each dominated by a different nannoplankton species. We suggest these shifts were linked to changes in how efficiently carbon was transported from the surface to the deep ocean. Comparing our results with other Northern Hemisphere sites shows that recovery patterns depended on distance from shore. In deeper open-ocean settings, nannoplankton species increased in size earlier than in shallower coastal areas. Because larger shells sink faster and enhance carbon transport, our findings suggest that both nannoplankton communities and the carbon cycle recovered more quickly in the open ocean than nearshore environments.

Key Points

- Nannoplankton boom-bust successions lasted for >~3.7 million years after the Cretaceous/Paleogene mass extinction at El Kef, Tunisia.
- A global comparison reveals that the exact sequence of taxa within boom-bust successions was primarily controlled by paleobathymetry.
- Paleobathymetric variability in boom-bust succession duration and cell size is likely intrinsically tied to biological pump recovery rates

1. Introduction

The bolide impact at the Cretaceous/Paleogene (K/Pg) boundary ca. 66 million years ago (Ma) – which most famously wiped out all non-avian dinosaurs (e.g., Alvarez et al., 1980; Chiarenza et al., 2020; Hull et al., 2020; Morgan et al., 2022; Schulte et al., 2010;) – also led to the largest mass extinction in the evolutionary history of calcifying marine plankton (i.e., calcareous nannoplankton and planktic foraminifera) with >90% species being eliminated (e.g., Bown et al., 2004; Fraass et al., 2015; Lowery et al., 2020; Molina et al., 1998; Perch-Nielsen et al., 1982; Thierstein, 1982). In comparison to marine calcifiers, siliceous and organic-walled plankton groups such as diatoms, radiolarians and dinoflagellates, suffered much lower extinction rates, likely due to the ability of some species to form resting cysts (Lowery et al., 2020; MacRae et al., 1996; Sims et al., 2006). Calcareous organisms living at the seafloor (e.g., benthic foraminifera) also did not experience a mass extinction at this time (e.g., Alegret & Thomas, 2013; Alegret et al., 2012, 2022; Culver, 2003; Thomas, 1990), underscoring that the K/Pg extinction predominantly affected marine calcifiers living in the upper water column (e.g., Lowery et al., 2020). This high level of extinction selectivity suggests that short-lived, impact-induced surface ocean acidification may have been an important kill mechanism (Brugger et al., 2021; Henehan et al., 2019) with impact-winter and decreased light availability caused by the emission of dust and aerosols also likely playing a major role (e.g., Brugger et al., 2021; Junium et al., 2022; Lyons et al., 2020; Morgan et al., 2022; Senel et al., 2023; Vellekoop et al., 2014).

As the most prolific and diverse phytoplankton group at the end of the Cretaceous (Knoll & Follows 2016; Lowery et al., 2020), the near-demise of calcareous nannoplankton at the K/Pg boundary had a major impact on marine ecosystem structure and function. Although primary productivity did not completely cease as originally proposed in the 'Strangelove Ocean' model (Hsü & McKenzie, 1985) and may have only been reduced by <50 % for less than a few tens of kyr (Henehan et al., 2019), vacated niche space in the photic zone was filled by alternative phytoplankton groups including dinoflagellates, diatoms and cyanobacteria (e.g., Alegret et al., 2022; Bralower et al., 2020; Lowery et al., 2021;

Renaudie et al., 2018; Schaefer et al., 2020; Sepúlveda et al., 2009; Vellekoop et al., 2017). The increased contribution of organic-walled phytoplankton to surface ocean productivity would have produced lower-density marine aggregates than those at the end of the Cretaceous, which were dominated by the heavily-mineralized remains of calcareous nannoplankton and planktic foraminifera. Moreover, because silica-producing diatoms did not become globally prominent until much later in the Cenozoic (~40 Ma), their role in early Paleocene marine carbon cycling was likely far less significant than in the modern ocean (e.g., Cermeño, 2016; Knoll & Follows 2016). This – together with the mass extinction's removal of aggregate-forming organisms at higher tropic levels – severely reduced biological pump efficiency (i.e., the 'Living Ocean' Model; Alvarez et al., 2019; Birch et al., 2016; Coxall et al., 2006; D'Hondt et al., 1998), which we define here as the proportion of carbon fixed during photosynthesis that is subsequently exported from the photic zone (after e.g., Ducklow et al., 2001; Henson et al., 2011; Hilting et al., 2008). In contrast, biological pump strength refers to the absolute flux of organic carbon exported from the surface to the deep ocean (Hilting et al., 2008).

Although the mass extinction exerted a global influence on biological pump strength and efficiency, its effects were geographically and environmentally heterogenous. This variability is reflected in site-to-site differences in both the magnitude and direction of benthic foraminiferal accumulation rates and diversity, which are strongly contrilled by the quantity and quality of organic matter exported from the surface ocean to the deep sea (e.g., Alegret & Thomas, 2009, 2013; Alegret et al., 2012, 2022; Hull & Norris, 2011; Sepúlveda et al., 2019). Similarly, export production, as inferred from excess barium, exhibits pronounced geographic variability across the K/Pg boundary (Hull & Norris, 2011). This so-called 'Heterogenous Ocean' (Alegret et al., 2022; Esmeray-Senlet et al., 2015; Henehan et al., 2019) likely reflects taxonomic differences associated with spatially and temporally restricted blooms of non-mineralizing phytoplankton, which may have been unable to efficiently exploit elevated surface ocean nutrients in formerly nutrient-poor regions, although this has not been thoroughly documented (Alegret et al., 2022; Bralower et al., 2020).

The recovery patterns of calcareous nannoplankton communities during the early Danian were similarly complex. In the Southern Hemisphere, nannoplankton extinction rates were somewhat lower than in the Northern Hemisphere (Jiang et al., 2010) and earliest Paleocene communities consisted of previously-rare survivor taxa that became regionally incumbent for 300 – 400 kyr post-impact (Jiang et al., 2010; Schueth et al., 2015). In contrast, contemporaneous Northern Hemisphere communities were characterized by a series of low-diversity, high-dominance acmes of newly-evolved taxa, which gave rise to the long-ranging lineages that prevailed throughout much of the Paleogene (Alvarez et al., 2019; Bown, 2005; Bown et al., 2023; Jiang et al., 2010, 2019; Jones et al., 2019; Schueth et al., 2015). Although these early Danian nannoplankton "boom-bust successions" (Jones et al., 2019) have been observed at all previously-studied Northern Hemisphere sites, their duration and the specific taxa that comprised them were geographically variable (Alvarez et al., 2019; Jones et al., 2019; Schueth et al., 2015). For example, boom bust successions ended ca. 1.75 Myr post-impact at Ocean Drilling Program (ODP) Site 1209 (Shatsky Rise) in the pelagic (bathyal) sub-equatorial Pacific Ocean (Alvarez et al., 2019), ca. 2 Myr post-impact at International Ocean Discovery Program (IODP) Site U1407 in the mid-latitude pelagic (abyssal) North Atlantic Ocean (Bown et al., 2023) and ca. 2.5 Myr post-impact at hemipelagic IODP – International Continental Scientific Ocean Drilling (ICDP) Site M0077A in the peak-

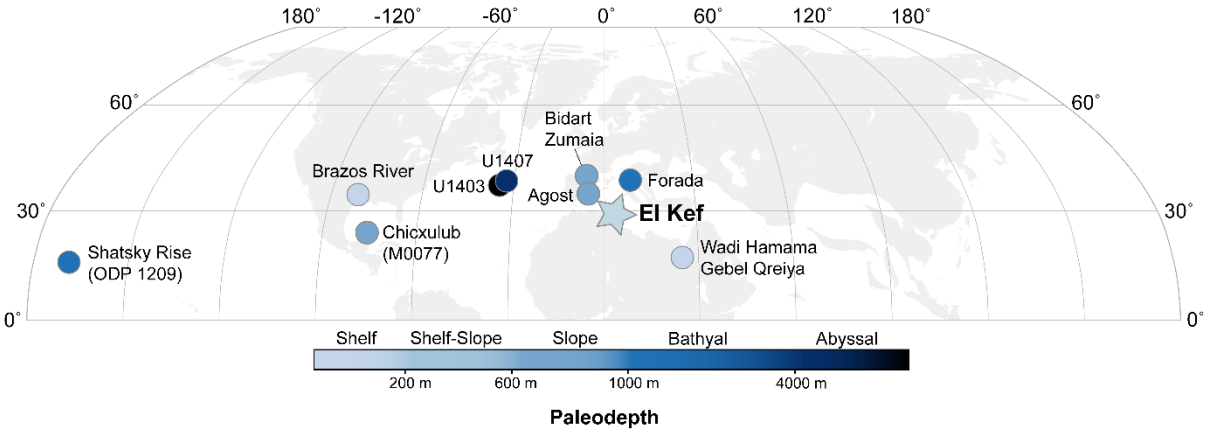

Figure 1. Paleogeographic reconstruction of the Northern Hemisphere at ~66.0 Ma showing the location of El Kef and other sites discussed in this study. Figure was created using pyGPlates (Mather et al. 2024) using the optimized plate model of Müller et al. (2022).

ring of the Chicxulub impact crater (i.e., at "ground-zero" of the mass extinction event; Jones et al., 2019; Lowery et al., 2021; Figure 1).

Although boom-bust successions are a distinctive feature of both calcareous nannoplankton and planktic foraminifera communities during the K/Pg recovery, the mechanisms controlling them are poorly understood (Alvarez et al., 2019; Bown, 2005; Hull, 2015; Hull et al., 2011; Jones et al., 2019). One hypothesis is that these patterns reflect a form of ecological succession analogous to that observed in modern ecosystems, but operating over much longer timescales (tens of thousands to millions of years), in a process referred to as Earth system succession (Hull, 2015). In this framework, a mass extinction event disrupts and destabilizes global biogeochemical cycling through both environmental perturbations and the loss of organisms that play key roles in these cycles (e.g., nannoplankton and planktic foraminifera), driving the Earth system into a state of disequilibrium. Therefore, boom-bust successions were likely a result of the complex biotic and abiotic interactions within the marine ecosystem as it progressively returned to relative equilibrium. These interactions may have included shifts in competitive advantage as environmental conditions and ecosystem function changed (e.g., Alvarez et al. 2019), modifications to feeding strategy (e.g., Gibbs et al. 2020) and changes in biological pump efficiency (Birch et al., 2016; 2021; Jones et al., 2019; Lowery et al., 2021).

Given the pronounced geographic heterogeneity in paleoecological, paleoenvironmental, and biogeochemical responses to the K/Pg mass extinction, global variation in the taxonomic composition and duration of nannoplankton boom-bust successions is hardly surprising. However, these differences and their dominant controls have not been systematically explored. Here we present high-resolution calcareous nannofossil assemblage data from the expanded post-extinction interval in sediment cores recovered near the Global Stratotype Section and Point (GSSP) for the basal Danian at El Kef, Tunisia. This record provides the most complete outer-shelf documentation of post-K/Pg nannoplankton boom-bust successions to date, allowing us to begin identifying the primary controls on these unique assemblages. Furthermore, statistical comparison of these data with those from other Northern Hemisphere sites are able to better resolve spatial patterns in the taxonomic composition and duration of boom-bust successions, providing new insight into Earth system recovery following the most recent mass extinction event.

2. Methods

2.1 Study site

During the El Kef Coring Project, sediment cores were recovered from five closely spaced holes (Holes A-E) drilled near the GSSP outcrop section, ~5 km southwest of the town of El Kef in northwestern Tunisia (Jones et al., 2023). Because of the drilling process, diagnostic features of the K/Pg boundary observed in the El Kef outcrop (e.g., the 2-3 mm iridium lamina) were not preserved in the cores. Nevertheless, integration of biostratigraphic, geochemical, and X-Ray Fluorescence (XRF) data allowed precise delineation of the boundary and the construction of a composite stratigraphic section ('splice') (Jones et al., 2023).

The resulting preferred age model indicates that the Danian succession is nearly complete in the El Kef cores, with the exception of a single unconformity within planktic foraminiferal biozone P1b. This unconformity is recognized by a sharp lithological contact and abrupt shifts across multiple geochemical records (Jones et al., 2023). Although the duration of the unconformity cannot be tightly constrained due to the absence of within-biozone tie points, sedimentation-rate estimates suggest it was ~500 kyr. As the early Danian at El Kef is characterized by a progressive decrease in sedimentation rates, this unconformity may represent an interval of reduced sediment accumulation or non-deposition, potentially linked to sea-level rise associated with the reactivation of syndepositional faulting. The Danian sediments at El Kef predominantly consist of gray marls (carbonate-rich mudstones) that are darker in color and less heavily bioturbated below the unconformity (Jones et al., 2023). The entire section was deposited at a paleolatitude of 25-30°N on the Tunisian outer continental shelf to upper ramp, at an estimated paleodepth of ~200-600 m (Figure 1; Alegret et al., 2022).

2.2 Age model revision

The current preferred age model for the El Kef cores (Jones et al., 2023) is primarily constrained by planktic foraminiferal biostratigraphic datums and is regarded as robust for the early Danian (biozones P0 through the base of P1b). Above this interval, however, its reliability declines due to challenges in identifying key biozone markers immediately above the unconformity in Hole E, as a result of poor preservation, weathering and reworking. There were also some difficulties in precisely delineating the base of biozone P2 in Hole C, where the defining marker taxon *Praemurica uncinata* is rare and exhibits a discontinuous occurrence (Jones et al., 2023). This issue is likely exacerbated by methodological constraints, as biozone determinations were based solely on the 38–63 µm size fraction due to sampling restrictions during the COVID-19 pandemic. Therefore, the larger specimens that became increasingly more common during the Danian, may not have been observed.

To further improve the reliability of our age model, planktic foraminiferal biostratigraphy was conducted on the >75 µm size fraction for 28 samples from El Kef Hole C and 44 samples from El Kef Hole E. The specific purpose of these additional analyses was to better constrain the base of biozone P2 and the timing of the unconformity, whilst ensuring biostratigraphic consistency between different size fractions during the earlier Danian (i.e., biozones P0 through P1b). Samples were soaked in a solution of peroxide and borax for a minimum of 24 hours and then washed over a 45µm sieve. In-between samples the sieve was soaked in methylene blue dye to mark any contamination. The washed samples were then dried overnight in a 40 °C oven. Each sample was sieved at 75 µm and analyzed under a Zeiss Discovery V8 microscope for presence/absence of biostratigraphic markers using the biozonation scheme of Wade et al (2011), with ages calibrated to CENOGRID (Westerhold et al. 2020).

2.3 Calcareous nannofossil assemblage counts

Using the El Kef age model and composite section (Jones et al., 2023) as a guide, we chose to use samples from Holes E and C, as combined these represent a nearly stratigraphically continuous K/Pg succession from immediately after the mass extinction event to the base of the *Futyania* acme (planktic foraminiferal biozones P0 to P1c; Hole E), and from the *Futyania* acme to the *Praeprinsius* acme (planktic foraminiferal biozones P1c and P2; Hole C). Nannofossil smear slides were made following the standard procedures outlined in Bown & Young (1998) and examined under cross-polarized light at 1600x magnification. Smear slides were analyzed at a 10 to 20 cm sampling resolution between 54.75 and 61.33 meters composite depth (mcd), a 10 to 20 cm sampling resolution between 35.88 and 54.75 mcd, and a sampling resolution of 60 cm above this (17.47 – 35.88 mcd) (Jones et al., 2023). Because the switchovers between boom-bust successions were geologically rapid events followed by a relatively prolonged interval of quasi-stability, we do not anticipate that the stratigraphic reduction in sampling resolution up-section has drastically altered our results or interpretations. Nannofossil assemblages in the weathered intervals of Holes C and E (above 17.47 mcd and 51.32 mcd respectively) were also examined, but are not included in the subsequent analyses due to clear downhole contamination and poor nannofossil preservation.

At least 300 nannofossil specimens were counted along a random transect in each sample and identified to species-level using the taxonomic concepts of Bown et al. (2023). Replicate counts were also implemented for most samples along a different random transect to improve reliability of the data. Some specimens, including tiny (<2 μm) *Neobiscutum* coccoliths and intermediate, evolutionary morphotypes of all incoming taxa were difficult to identify to species-level, and thus were only assigned a genus. Ultimately, our nannoplankton relative abundance counts resulted in the creation of a large dataset comprising of 186 samples and over 104,000 nannofossil occurrences.

2.4 Statistical analyses

All statistical analyses were conducted on genus-level data, allowing for more reliable comparison of the nannofossil assemblage records compiled by different nannofossil workers whilst still showing meaningful paleoecological trends. Only genera that comprised >2% of an assemblage were included in statistical analyses to limit the formation of outliers that obscure primary paleoecological signals (e.g., Schneider et al. 2013). A Hellinger transformation was then applied to the genus-level assemblage data using the *vegan* package (Oksanen et al., 2025) in R Version 4.5.1 (R Core Team, 2025). This transformation first standardizes the data by the sample size (i.e. divides all values in a row by the row sum), which accounts for differences in the total number of specimens counted per sample. It then takes the square root of the values to maximize the importance of rare taxa. This is vital in teasing apart differences between assemblages that are almost completely dominated by one abundant taxon, as is the case within the early Danian boom-bust successions.

2.4.1 Single-site Nonmetric Multidimensional Scaling (NMDS): To statistically analyze the temporal changes in nannofossil assemblages at El Kef, we performed NMDS using the 'metaMDS' function within R's *vegan* package (Oksanen et al., 2025; R Core Team 2025). This iterative ordination technique uses a distance measure (in this case the Bray-Curtis distance) to find a best-fit rank distance matrix in a reduced axis space. The number of axes (dimensions) used is specific to each data matrix and is manually chosen by the user when the 'stress' value is reduced to a point where it plateaus (in this case 3 dimensions). After running the NMDS, the 'metaMDS' function performs a principal components analysis of the sample scores to rotate them into a maximum variance orientation. Species scores are

determined by weighted averaging using the function 'wascores'. Each point on the resulting ordination plot represents the nannofossil assemblage of a single sample, with closer points indicating more similar assemblages. NMDS axis 1 explains the most variability between samples, followed by axes 2, 3, and so on. Although the paleoenvironmental and/or paleoecological controls represented by these axes cannot be determined directly from the ordination alone, samples can be coded by associated parameters (e.g., geochemical data, age, or site location when multiple sites are included). This allows NMDS to help identify the external factors most strongly influencing changes in nannofossil assemblage composition across large datasets.

We performed three separate NMDS analyses: one using nannofossil assemblage data from both Holes E and C, one only using assemblage data from Hole E and the last only using data from Hole C. To test whether changes in nannofossil assemblages and paleoenvironmental variables were correlated, we performed a linear regression of the available geochemical data (bulk carbonate $\delta^{13}C$ and $\delta^{18}O$, bulk organic $\delta^{13}C$, % TOC, and % $CaCO_3$; Jones et al., 2023) on the NMDS sample scores using the 'envfit' function in the *vegan* package in R (Oksanen et al.2025; R Core Team 2025). Because geochemical measurements were not always conducted on the same samples as the nannofossil assemblage counts, we linearly interpolated geochemical values for each nannofossil sample. Specifically, each missing geochemical value was estimated using the two nearest measured points in the section (one above and one below), assuming a linear change between them. The NMDS and 'envfit' results were then plotted together using the *ggplot2* package (Wickham et al., 2016).

2.4.2 Spearman's Rank correlation plots: Changes in nannofossil assemblages and geochemical proxy data may be decoupled, and only appear to be correlated due to independently-controlled stratigraphic trends. For this reason, the Spearman's rank correlation coefficients between all pairs of columns within a matrix – including relative abundances of the major nannofossil acme taxa, all available geochemical proxy data, and time (in Ma) – were calculated using the 'rcorr' function within the *Hmisc* package in R (Harrell, 2025; R Core Team 2025). The pairwise correlation matrices were then visualized using the *corrplot* package (Wei & Simko, 2024).

2.4.3 Regional two-way hierarchical cluster analysis: To determine the extent to which regional paleoceanographic conditions played a role in the recovery of calcareous nannoplankton, we performed a two-way cluster analysis using the nannofossil assemblage data from El Kef and six other Tethyan sites from the literature (Figure 2): Bidart, France (Jiang et al., 2019); Zumaia, Spain (Jiang et al., 2019); Agost, Spain (Jiang et al. 2010); Forada, Italy (Fornaciari et al., 2007); Wadi Hamama, Egypt (Tantawy, 2003) and Gebel Qreiya, Egypt (Tantawy, 2003). Due to the temporal constraints and low-resolution age models of many of the published sites, statistical analyses were restricted to data spanning the first ~3.5 Myr of the Danian. The two-way cluster analysis was performed using the Bray-Curtis distance measure and Ward's linkage method within the *pheatmap* package in R (Kolde 2025). This creates a dendrogram of genera on the x axis and samples on the y axis, with taxa clustering based on co-occurrence among samples, and samples clustering due to similarities in nannofossil assemblage composition.

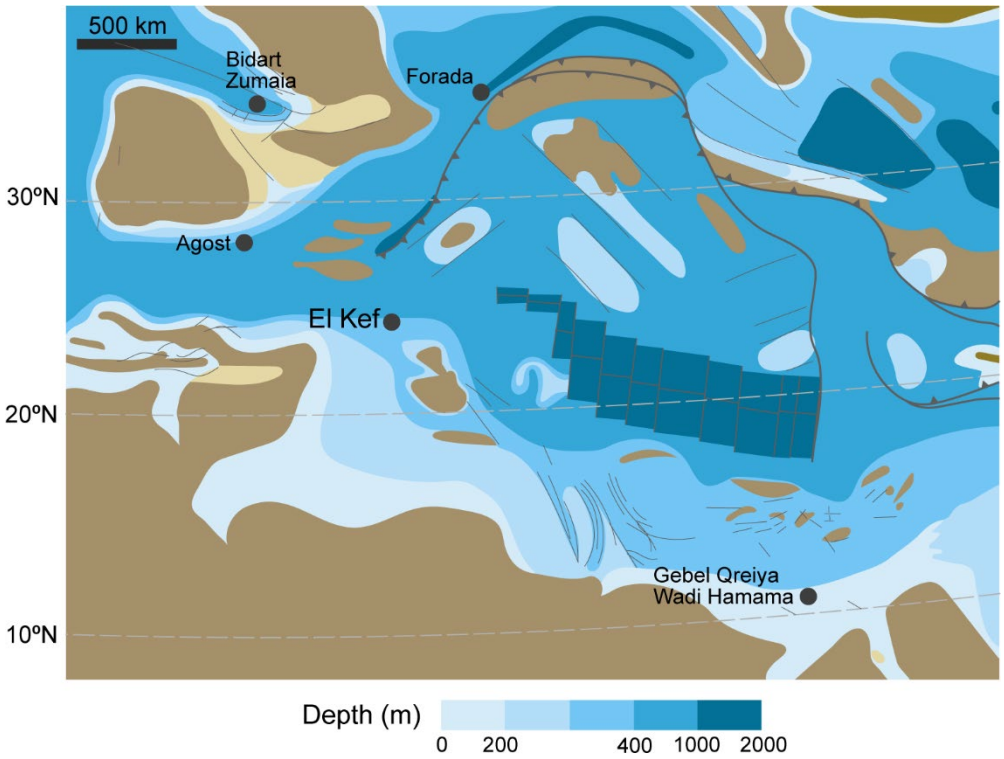

Figure 2. Paleogeographic reconstruction of the peri-Tethys region during the late Maastrichtian, showing the approximate location of El Kef relative to the other Tethyan sites statistically analyzed in this study. Modified from Fornaciari et al., 2007 and Philip & Floquet, 2000.

2.4.4 Northern Hemisphere NMDS: To compare changes in nannofossil assemblages at El Kef to those at other Northern Hemisphere sites, we compiled a dataset using results published in the literature, which sample several different ocean basins and marine environments (Figure 1). In addition to the Tethyan sites listed in Section 2.4.3, five additional sites are included in this Northern Hemisphere dataset: IODP-ICDP Site M0077A in the peak ring of the Chicxulub impact crater, Mexico (Jones et al., 2019); Brazos River, Texas, USA (Schueth, 2009); Shatsky Rise (ODP Site 1209), North Pacific Ocean (Alvarez et al., 2019) and IODP Sites U1403 and U1407 in the North Atlantic Ocean (Bown et al., 2023). As in the two-way hierarchical cluster analysis (Section 2.4.3), only data spanning the first ~3.5 Myr of the Danian were used in the NMDS analysis, which was conducted and visualized as an ordination plot using the *vegan* and *ggplot2* packages respectively (Oksanen et al. 2025; Wickham et al., 2016).

3. Results

3.1 Revised El Kef age model

Planktic foraminifera in the > 75 µm size fraction are relatively well preserved. As expected, our revised biostratigraphy shows substantial differences in the delineation of the two youngest biozones, P1c and P2, with additional minor adjustments to the bases of P1a and P1b (Table 1; Jones et al. 2023). Delineation of biozones P0 and Pα remains unchanged from the original age model (Jones et al. 2023). However, recently-published ^{3}He isotopic data (Lowery et al., 2026) – including from the El Kef outcrop section – indicate a much shorter duration for P0 (~6.61 kyr) than previously estimated (~30 kyr), requiring revision of the P0-Pα age model (Table 1). These updates imply very high average sedimentation rates during P0 (~12.4 cm/kyr), declining to ~1.7 cm/kyr in Pα and ~0.18-0.22 cm/kyr through P1a-P1b, before increasing slightly in P1c (~0.45 cm/kyr). The very low sedimentation rates in P1b and P1c are consistent with the inferred unconformity, reflecting a possible interval of non-deposition or erosion associated with sea-level rise.

Definitive *Globanomalina compressa* specimens (marker for the base of biozone P1c) and secondary P1c indicators such as *Praemurica inconstans* and *Parasubbotina varianta* were observed within multiple samples at the base of El Kef Hole E Core 4R, 90 to 150 cm (51.32 to 51.92 mcd), which were not previously examined for planktic foraminiferal biostratigraphy (Jones et al. 2023). These samples are from below the heavily weathered/oxidized depth interval that ranges from the top of Hole E to Hole E Core 4R, ~81 cm (46.18 to 51.23 mcd; Jones et al. 2023), indicating that the presence of these taxa is likely a primary signal and not a product of downhole contamination or mixing. These new observations push the depth of base P1c – which was previously placed in a sampling gap between the base of Hole C and top of Hole E Core 5 (~50.63 mcd; Jones et al. 2023) – down to 52.16 mcd (Table 1), which also greatly reduces the error associated with its delineation (from +/- 1.53 m in Jones et al. (2023) to +/- 0.24 m in this study; Table 1). Although this improves the reliability of the El Kef age model, it also means that the unconformity may also include the lowest part of P1c in addition to the upper part of P1b, making it longer than initially estimated (i.e., >500 kyr; Jones et al. 2023). Unfortunately, it is currently unknown exactly how much time is missing from the base of P1c. As only 5 nannofossil samples were counted above the unconformity in Hole E, this uncertainty will not significantly alter our discussion on recovery dynamics, as the remainder of Holes E and C have relatively reliable age control. However, future studies should aim to constrain the length of this unconformity by conducting further stratigraphic work on El Kef Hole D: the only other hole that preserves the unconformable contact (Jones et al. 2023).

Biozone	Event	Age estimate (Ma)	Age source	Top sample ID	Top sample depth (mcd)	Bottom sample ID	Bottom sample depth (mcd)	Midpoint depth (mcd)	± (m)
P2	B *Praemurica uncinata*	62.537	Wade et al. (2011); Gradstein et al. (2012); Westerhold et al. (2020)	El Kef C 21R-1, 102-105 cm	45.44	El Kef C 21R-1, 141-144 cm	45.83	45.64	0.20
P1c	B *Globanomalina compressa*	63.978	Wade et al. (2011); Gradstein et al. (2012); Westerhold et al. (2020)	El Kef E 4R-1, 150 cm	51.92	El Kef E 5R-1, 34 cm	52.39	52.16	0.24
P1b	B *Subbotina triloculinoides*	65.184	Wade et al. (2011); Gradstein et al. (2012); Westerhold et al. (2020)	El Kef E 6R-1, 100-101 cm	54.66	El Kef E 6R-1, 120-121 cm	54.86	54.76	0.10
P1a	T *Parvularugoglobigerina eugubina*	65.690	Wade et al. (2011); Gradstein et al. (2012); Westerhold et al. (2020)	El Kef E 7R-1, 30-31 cm	55.60	El Kef E 7R-1, 45-46 cm	55.75	55.68	0.08
Pα	B *Parvularugoglobigerina eugubina*	66.015	Lowery et al. (2026)	El Kef E 10R-1, 70-72 cm	60.99	El Kef E 10R-1, 84-86 cm	61.13	61.06	0.07
P0	T Cretaceous taxa	66.022	Dinares-Turell et al. (2014)	El Kef E 10R-1, 139-140 cm	61.68	El Kef E 11R-1, 1-2.5 cm	62.08	61.88	0.20

Table 1. Updated planktic foraminiferal biostratigraphic zonations for the El Kef composite core section in Holes C and E, with depth in metres composite core depth (mcd).

The base of P2 was also found to be much lower in this study (~45.64 mcd) than in the initial age model (~34.04 mcd), probably due to increased relative rarity of the P2 marker taxon *Praemurica uncinata* within the smaller size fraction (38-63 µm) examined in Jones et al. (2023) compared to the >75 µm size fraction examined here (Table 1). This is supported by the fact that very rare *P. uncinata* specimens were also observed lower in Hole C (~43.75 mcd) within the 38-63 µm size fraction, but were interpreted as downhole contamination due to the continuous absence of this taxon within samples from the ~10 m depth interval above this. However, based on our new data from the >75 µm size fraction, the rare *P.uncinata* specimens observed in the 38-63 µm size fraction were actually likely in situ and representative of the smaller forms typical for a species at the beginning of its stratigraphic range. In this case, the exclusion of *P. uncinata* from the 38-63 µm size fraction samples in the overlying 10 m of sediments may be indicative of their rapid evolution to larger average test sizes, with their

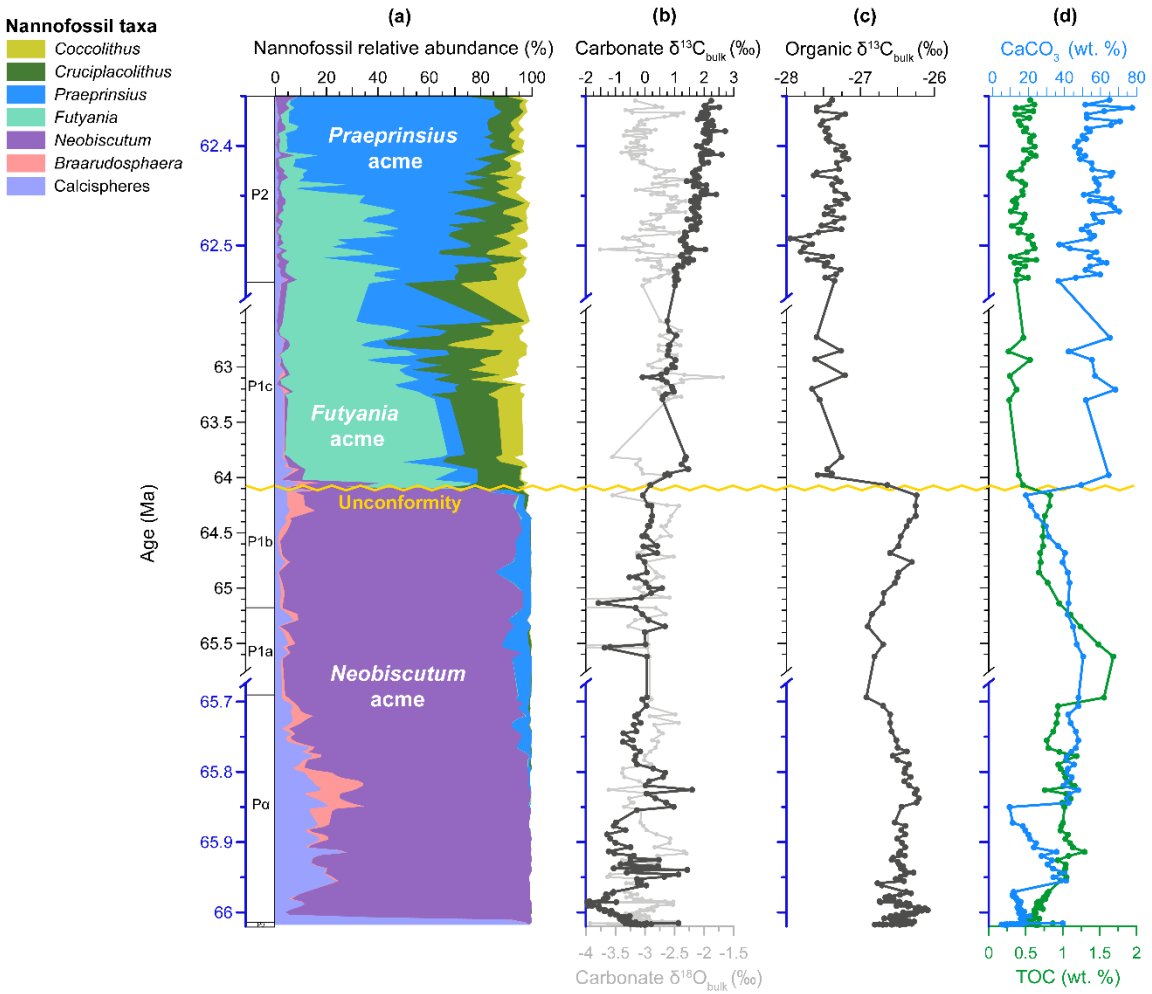

Figure 3. Nannofossil and geochemical records from ~62.35 – 66.02 Ma in sediment cores from El Kef, Tunisia alongside the planktic foraminiferal biozones. Note the two y-axis scale changes (blue), reflecting comparatively high sedimentation rates in P0-Pα and P2. Because the duration of the unconformity (yellow line) is unconstrained, sedimentation rates are calculated assuming continuous deposition across the contact, although this likely does not reflect the true depositional history. (a) Cumulative frequency plot showing the relative abundance of the seven most abundant nannofossil taxa. (b) Bulk carbonate $\delta^{13}C$ (black) and $\delta^{18}O$ (light gray). (c) Bulk organic $\delta^{13}C$. (d) Coulometric measurements of weight % calcium carbonate ($CaCO_3$; blue) and wt. % Total Organic Carbon (TOC; green).

reappearance in the smaller size fraction at ~34.04 mcd representing their increased relative abundance in assemblages and/or their diversification to encompass a wider range of test sizes.

The marker for the base of planktic foraminiferal zone P3 (*Morozovella angulata*) was not observed in either the 38-63 µm size fraction (examined up to El Kef Hole C 2R, 46-48 cm; Jones et al. 2023) or the >75 µm size fraction in the highest examined sample (El Kef Hole C 5R, 73-76 cm). Accordingly, the entire interval between ~14.32 and 45.64 mcd is assigned to biozone P2, which spans ~207,000 years (62.33 to 62.54 Ma; Gradstein et al., 2012; Wade et al., 2011; Westerhold et al., 2020). For this study, we assume 14.32 mcd represents the uppermost part of P2 (i.e., 62.33 Ma; the minimum age). This assumption implies unusually high sedimentation rates (~15.1 cm/kyr) within P2, which is unlikely, given the very low rates inferred below. However, because no additional (bio)stratigraphic datums

occur within P2, the youngest part of the age model cannot be further constrained, and ages assigned to samples within P2 (i.e., <62.54 Ma) should therefore be treated with caution.

3.2 El Kef nannofossil relative abundance data

Overall, the revised El Kef age model indicates that our new nannofossil assemblage data spans the first ~3.7 Myrs of the Danian (Figure 3). Immediately after the K/Pg impact, nannofossils are almost completely absent due to their mass extinction, with assemblages comprising of reworked Cretaceous specimens and the calcareous resting cysts (calcispheres) of dinoflagellates, assigned to *Cervisiella* spp. However, these 'disaster' assemblages only lasted for ~11 kyr, before being replaced by *Neobiscutum*: the first of the incoming Paleocene nannoplankton taxa. *Neobiscutum* immediately dominated assemblages, with these communities persisting for 1.88 Myr (Figure 3a). Within this interval, the relative abundance of the nannolith taxon *Braarudosphaera* peaks at ~65.8 Ma, which coincides with an increase in bulk carbonate $\delta^{13}C$ (Figure 3b) and weight percent (%) calcium carbonate ($CaCO_3$; Figure 3d). The subsequent decrease in the relative abundance of *Braarudosphaera* (Figure 3a) is associated with: (a) the continued decline of *Cervisiella* spp.; (b) the increased abundance of tiny, ancestral *Praeprinsius* spp. (incl. *P.* cf. *vegrandis*; Bown et al. 2023), (c) decreasing trends in both bulk carbonate and bulk organic $\delta^{13}C$ values (Figure 3b; c) and; (d) an overall increase in weight % Total Organic Carbon (TOC; Figure 3d). The remainder of the *Neobiscutum* acme (~64.11 Ma – 65.7 Ma) is characterized by quasi-stable nannofossil assemblages (Figure 3a) and bulk carbonate $\delta^{13}C$ values (Figure 3b), a gradual increase in bulk organic $\delta^{13}C$ (Figure 3c) and a slow decline in both wt. % $CaCO_3$ and TOC (Figure 3d).

At ~64.1 Ma, there is a transition from the *Neobiscutum* acme to the *Futyania* acme (Figure 3a). Although this taxonomic switchover appears abrupt, it occurred across the unconformity in El Kef Hole E. Therefore, as this hiatus may represent more than 500 kyr, it is likely that this transition was actually more gradual that it appears. Overall, the *Futyania* acme is associated with the increased relative abundance of long-ranging Paleocene taxa *Cruciplacolithus* and *Coccolithus*, a large increase in bulk carbonate $\delta^{13}C$ (~1.5‰) and wt. % $CaCO_3$ (30%) and a decrease in bulk organic $\delta^{13}C$ and wt. % TOC. The next 1.5 Myr (~62.6 – 64.1) marks an interval of quasi-stability both in terms of nannofossil assemblage composition (Figure 3a) and surface ocean paleoenvironmental conditions as indicated by the stable isotope and coulometric data (Figure 3b-d). Beginning at ca. 62.6 Ma, there was a gradual dominance switchover between *Futyania* and *Praeprinsius*, with a definitive *Praeprinsius* acme becoming fully established by 62.46 Ma. The transition between the *Futyania* and *Praeprinsius* acmes is associated with: (a) a decline in *Cruciplacolithus* and *Coccolithus*, which had previously greatly increased in relative abundance within the *Futyania* acme; (b) a steady ~1.25‰ increase in bulk carbonate $\delta^{13}C$ to the top of the record (~62.35 Ma; Figure 1b); (c) a small negative excursion in bulk organic $\delta^{13}C$; and (d) a sharp decrease from ~65% to 40% weight % $CaCO_3$ at the beginning of the *Futyania* - *Praeprinsius* switchover, followed by highly variable values (35 to 75% wt. % $CaCO_3$) to the top of the examined interval (62.35 to 62.55 Ma; Figure 3d).

3.3 El Kef NMDS and correlation plots

The El Kef NMDS results (Figure 4) confirm four distinct generic acmes that define the boom-bust successions observed in the relative abundance data (Figure 3a): (1) the short lived *Cervisiella* acme, (2) the *Neobiscutum* acme, (3) the *Futyania* acme, and (4) the *Praeprinsius* acme. Overall, the largest change in nannofossil assemblages occurred between the *Neobiscutum* and *Futyania* acmes as

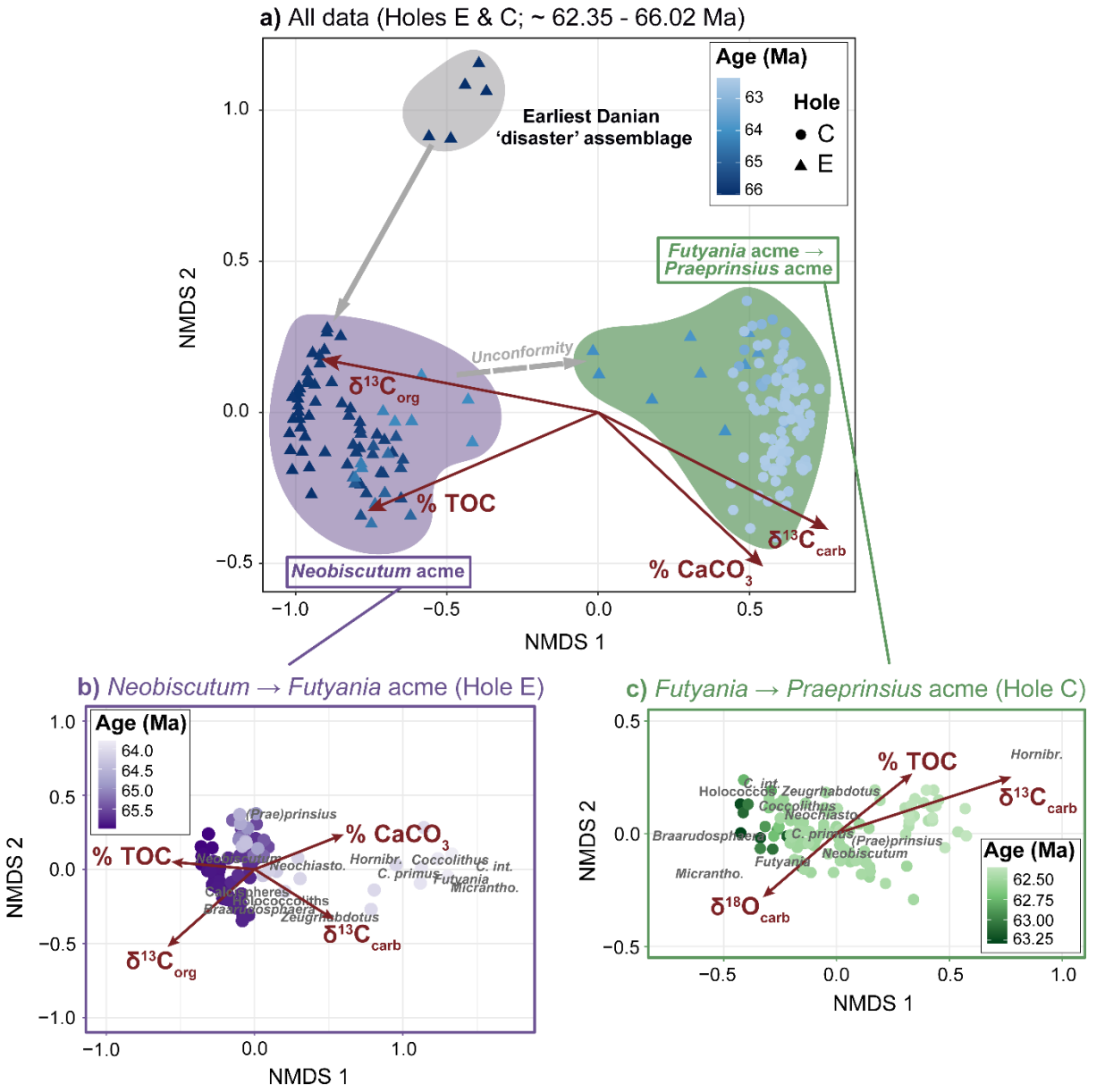

Figure 4. Nonmetric multidimensional scaling (NMDS) ordination plots showing the differences between nannofossil assemblages at El Kef. Points (sample scores) that are closer together in ordination space have more similar nannofossil assemblages that those that are further apart. The red vectors on each ordination show the regression ("environmental fit") of the geochemical data on the NMDS scores. The length of each of the vectors correspond to the strength of each of these correlations, with only statistically significant relationships ($p<0.01$) shown. (a) NMDS results for all nannofossil data (~62.35 – 66.02 Ma). (b) NMDS results for the subset of nannofossil data within Hole E, excluding the oldest five samples (~63.79 – 65.99 Ma). (c) NMDS results for the subset of nannofossil data within Hole C (~62.35 – 63.29 Ma).

indicated by increased sample scores along major NMDS axis 1 (Figure 4a). Changes in assemblage composition between the *Futyania* and *Praeprinsius* acme can be observed as a gradual decrease in NMDS axis 2 sample scores (Figure 4c), suggesting a subtler paleoecological transition compared to the *Neobiscutum*→ *Futyania* switchover (Figure 4b). The linear regression (environmental fit) of geochemical/coulometric data on the NMDS sample scores shows a statistically significant positive correlation with bulk carbonate $\delta^{13}C$ (r^2=0.7295, p=0.001) and wt. % $CaCO_3$ (r^2=0.5581, p=0.001), and a negative correlation with bulk organic $\delta^{13}C$ (r^2=0.8709, p=0.001) and wt. % TOC (r^2=0.6874, p=0.001),

primarily along NMDS axis 1. Subset analyses of the Hole E data (the *Neobiscutum* acme) reinforces these correlations albeit with lower r^2 values (r^2 = 0.4014, 0.4195, 0.6173 and 0.3181 for bulk carbonate $\delta^{13}C$, wt. % $CaCO_3$, bulk organic $\delta^{13}C$ and wt. % TOC respectively; Figure 4b), likely because the sediments within this hole contain the unconformable *Neobiscutum* → *Futyania* transition, which represents the largest paleoecological and paleoenvironmental transition within the entire El Kef record (Figure 4a). In contrast, the separate NMDS analysis for the Hole C samples – which contain the *Futyania* and *Praeprinsius* acmes – only shows a strong, statistically significant correlation with bulk carbonate $\delta^{13}C$ (r^2= 0.664, p=0.001) along NMDS axis 1 (Figure 4c). Interestingly, the strength of this correlation is higher than in the subset Hole E NMDS results (r^2= 0.4014, p=0.001; Figure 4b).

Because temporal trends strongly influence many variables, apparent correlations between different paleoecological and paleoenvironmental factors may not reflect direct relationships. In this case, correlation does not necessarily imply causation, as observed associations can arise simply because variables independently covary with time. To address this, we generated Spearman's rank correlation plots to examine pairwise relationships among multiple variables including estimated ages (Figure 5).

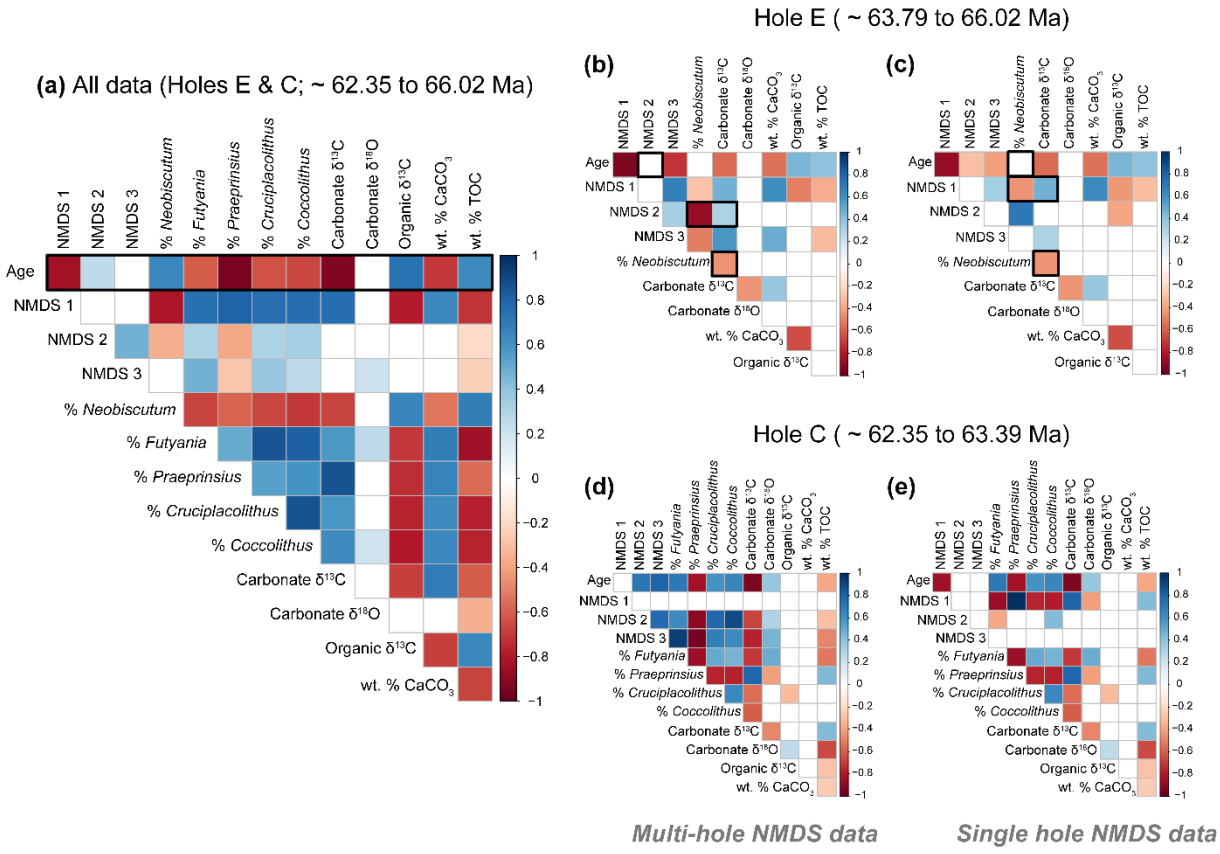

Figure 5. Spearman's rank correlation plots showing the strength of pairwise relationships between multiple variables. Positive relationships (r^2>0) are shown in shades of red, whilst negative relationships (r^2<0) are shown in shades of blue. Empty boxes (white) represent Spearman's rank correlations with a p value of less than 0.01. (a) Combination of all data from Holes E and C (~62.35 – 66.02 Ma). (b) Subset data from Hole E, with NMDS scores taken from the multi-hole analysis (i.e., Figure 4a; (~63.79 – 65.99 Ma)). (c) Subset data from Hole E, with NMDS scores taken from the Hole E single-hole analysis (i.e., Figure 4b; (~63.79 – 65.99 Ma)). (d) Subset data from Hole C, with NMDS scores taken from the multi-hole analysis (i.e., Figure 4a; (~62.35 – 63.29 Ma)). (e) Subset data from Hole C, with NMDS scores taken from the Hole C single-hole analysis (i.e., Figure 4c; (~62.35 – 63.29 Ma)).

As anticipated, the correlation plot based on NMDS axis scores for the complete El Kef dataset (Figure 4a) shows that all considered variables are strongly correlated with time (Figure 5a). This is simply due to the large amount of change that occurred during this volatile study interval, which complicates the interpretation of 'true' correlations between paleoecological and paleoenvironmental variables.

The examination of data from the two separate holes using NMDS axes for the complete El Kef dataset (Figure 5b,d) and those from the appropriate subset analyses (Figure 5c, e) show similar results. The one important exception is the apparent negative correlation between the relative abundance of *Neobiscutum* and bulk carbonate $\delta^{13}C$ (Figure 5b, c). In the case of the multi-hole statistical analysis (Figure 5b), NMDS axis 2 does not show a significant statistical correlation with time, but does with both % *Neobiscutum* and bulk carbonate $\delta^{13}C$. This is supported by the single-hole data (Figure 5c), which suggests that changes in the relative abundance of *Neobiscutum* are not significantly correlated to time but are negatively correlated to bulk carbonate $\delta^{13}C$. Although it is important to note that both of these variables are correlated to NMDS 1 axis values – which is itself strongly correlated to time – these results provide tentative evidence that changes in nannofossil assemblages within the *Neobiscutum* acme and during *the Neobiscutum* → *Futyania* switchover were directly linked to increased bulk carbonate $\delta^{13}C$ values. In contrast, the Hole C multi-site data (Figure 5d) shows that NDMS axis 1 is not significantly correlated to any of the variables, including time. Instead time is correlated with NMDS axis 2 – and even more so with NMDS axis 3 – which are both in turn correlated with most other considered paleoecological and paleoenvironmental parameters (excluding bulk organic $\delta^{13}C$ and wt. % $CaCO_3$). Although the single hole-analysis for Hole C indicates that time is not significantly correlated to NMDS axes 2 and 3 (Figure 5e), the relative abundance of *Futyania* and *Coccolithus* are the only variables that are significantly correlated with either of these axes. Therefore, it is not possible to make the same speculative link between changes in nannofossil assemblages and bulk carbonate $\delta^{13}C$ within the *Futyania* and *Praeprinsius* acmes as in the earlier *Neobiscutum* acme.

3.4 Regional cluster analysis

The two-way hierarchical cluster analysis conducted on our new El Kef data and additional published records from a range of other Tethyan sites, reveals three major clusters related to distinct nannofossil assemblages (Figure 6). Cluster 1 comprises of three sub-clusters and represents earliest Danian 'disaster' assemblages. Sub-Cluster 1A-I is characterized by the almost complete dominance of calcispheres within samples from Wadi Hamama and Gebel Qreiya (Egypt), as well as the oldest five samples from El Kef. Calcispheres also dominate the sub-Cluster 1A-II samples, but can be distinguished from sub-Cluster 1A-I by the relatively high abundance of Cretaceous survivor taxon *Cyclagelosphaera*. Samples from sub-Cluster 1A-II are predominantly from Bidart (France) and Zumaia (Spain), with one sample from Forada (Italy). Sub-Cluster 1B is characterized by a calcisphere acme with relatively high abundances of *Neobiscutum* and low holococcolith abundance (1B-I) or with a high relative abundance of *Braarudosphaera* (1B-II). Samples from the former are restricted to the Egyptian continental shelf sites Wadi Hamama and Gebel Qrieya, whilst the latter predominantly comprises of samples from Forada and Zumaia. The last sub-cluster within Cluster 1 consists of a *Braarudosphaera* acme with relatively high abundances of *Neobiscutum* and low abundances of calcispheres (samples from Zumaia, Agost, Wadi Hamama and Gebel Qrieya; sub-Cluster 1C-I) or a *Braarudosphaera* acme with relatively high abundances of *Cyclagelosphaera,* calcispheres, and/or holococcoliths and low abundances of *Neobiscutum* (samples from Bidart, Agost and Forada; sub-Cluster 1C-II). Samples from El Kef are completely absent from sub-Clusters 1B and 1C.

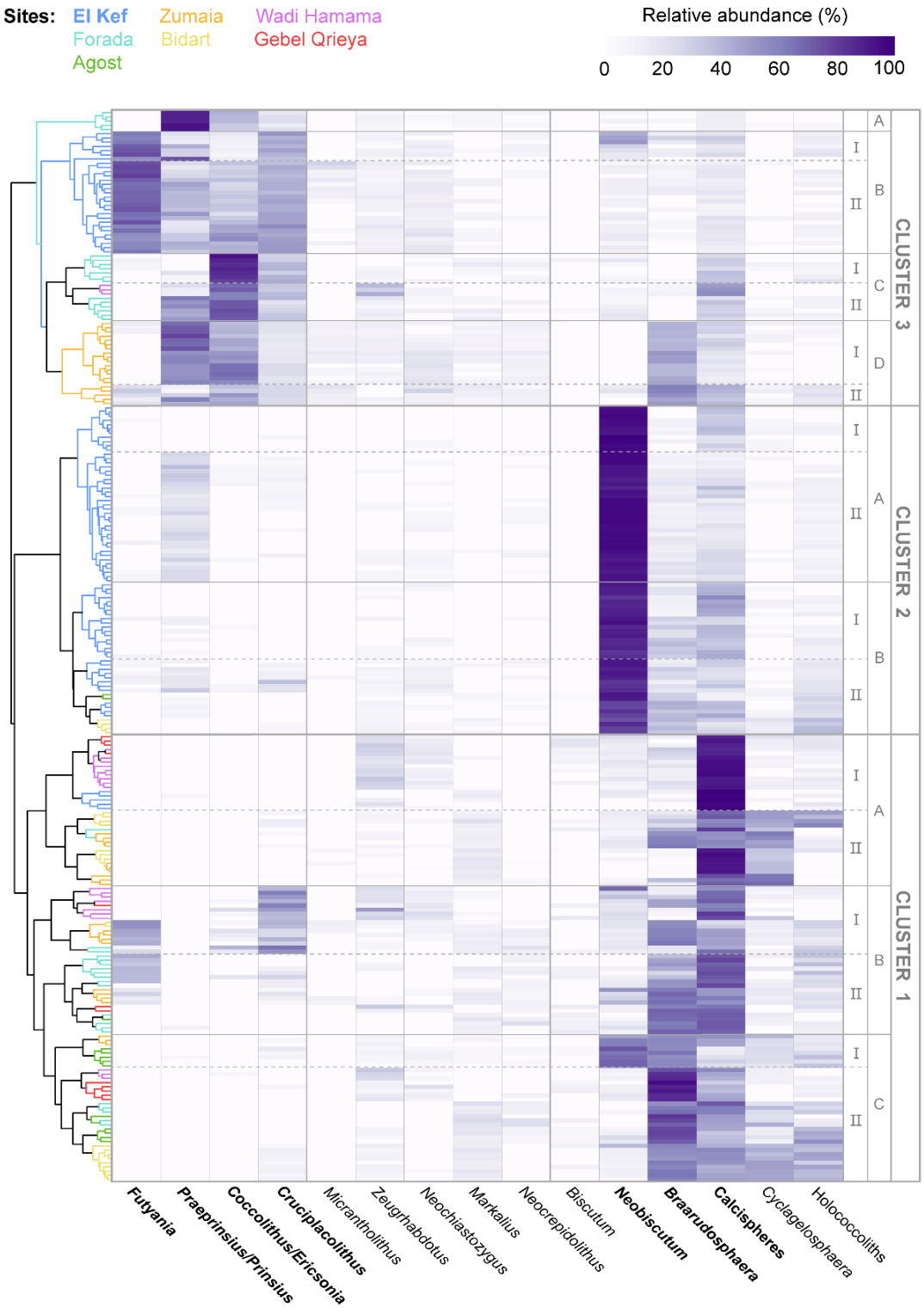

481

Figure 6. Dendrogram showing the results of a regional (Tethyan) two-way cluster analysis or 'heatmap' conducted on nannofossil relative abundance data. The horizontal (x-axis) dendrogram shows the clustering of nannofossil genera and the vertical (y-axis dendrogram) shows clustering between samples, with the site that the sample is from distinguished by color: blue = El Kef (this study), teal = Forada (Fornaciari et al. 2007), green = Agost (Jiang et al. 2010), orange = Zumaia (Jiang et al. 2019), yellow = Bidart (Jiang et al. 2019), pink = Wadi Hamama (Tantawy 2003) and red = Gebel Qrieya (Tantawy 2003). The relative abundances of nannofossil taxa are also shown in accordance with the scalebar to the top-right of the figure.

Cluster 2 represents the *Neobiscutum* acme and almost entirely consists of samples from El Kef (Figure 6). Sub-Cluster 2A is characterized by the very high abundance of *Neobiscutum* with a lower abundance of calcispheres (2A-I) or early *Praeprinsius* cf. *vegrandis* (2A-II). In comparison, samples within sub-Cluster 2B have slightly lower relative abundances of *Neobiscutum* with a higher proportion of calcispheres (2B-I) or with increased relative abundances of calcispheres, holococcoliths and *Braarudosphaera* (2B-II). Sub-Cluster 2B-II is the only group to contain samples that are not from El Kef (Agost and Bidart).

The last major cluster (Cluster 3) contains samples from the latest part of the K/Pg recovery interval included in this analysis. Sub-Cluster 3A represents the *Praeprinsius* acme at Forada, which also features lower abundances of *Coccolithus* and *Cruciplacolithus*. In contrast, sub-Cluster 3B – which only comprises samples from El Kef – is characterized by the *Futyania* acme, with relatively high abundances of *Cruciplacolithus*, variable abundances of *Praeprinsius* and either a very low (3B-I) or relatively high (3B-II) proportion of *Coccolithus*. Sub-Cluster 3C predominantly consists of samples from Forada, and is representative of a *Coccolithus* acme with a relatively high proportion of *Cruciplacolithus* and either a low (3C-I) or relatively high (3C-II) abundance of *Praeprinsius*. The last sub-Cluster (3D) only contains samples from Zumaia, and is characterized by a *Coccolithus* acme with a relatively high abundance of *Braarudosphaera* and either a higher proportion of *Praeprinsus* (3D-I) or comparatively higher relative abundances of calcispheres, holococcoliths and *Futyania* (3D-II).

3.5 Northern Hemisphere NMDS analysis

To compare Tethyan nannoplankton recovery patterns for the first ~3.5 Myr of the Danian to those in other Northern Hemisphere ocean basins, we conducted a further NMDS analysis with sample scores coded by both location (site and region; Figure 7a) and estimated paleobathymetry (Figure 7b). Our results reveal that the largest change in nannofossil assemblages – as observed along NMDS axis 1 – are associated with the transition from post-extinction acmes (high NMDS axis 1 scores) to the formation of more diverse communities (low NMDS axis 1 scores). However, it is important to note that within the examined 3.5 Myr time frame, only three open ocean sites – ODP Site 1209 (Shatsky Rise, subtropical Pacific Ocean) and IODP Sites U1403 & U1407 (mid-latitude North Atlantic Ocean) – completed the full transition to stable nannofossil assemblages comprising of long-ranging Paleocene taxa such as *Cruciplacolithus*, *Coccolithus*, *Toweius* and *Fasciculithus*.

The two major pathways leading to the establishment of stable assemblages are dependent on the immediate post-impact community composition (Figure 7a). For almost all of the Tethyan sites and IODP-ICDP Site 364 (Chicxulub impact crater, Gulf of Mexico), early nannofossil assemblages consist of relatively high abundances of calcispheres, *Braarudosphaera* and/or *Cyclagelosphaera,* with a stratigraphic transition to increased *Cruciplacolithus* and/or *Coccolithus* abundances. Alternatively, earliest Danian assemblages from El Kef, Brazos River (USA), ODP Site 1209 and IODP Site 1403 are characterized by a well-defined *Neobiscutum* acme. Although a few samples from Bidart and Agost also show an increased relative abundance of *Neobiscutum* during the recovery interval, this taxon does not form a true acme as at the aforementioned four sites. The short-lived *Neobiscutum* acme at both ODP Site 1209 and IODP Site U1403 is followed by a succession of dominance switchovers (*Cruciplacolithus* → *Praeprinsius* → *Coccolithus*) prior to the establishment of more permanent, stable

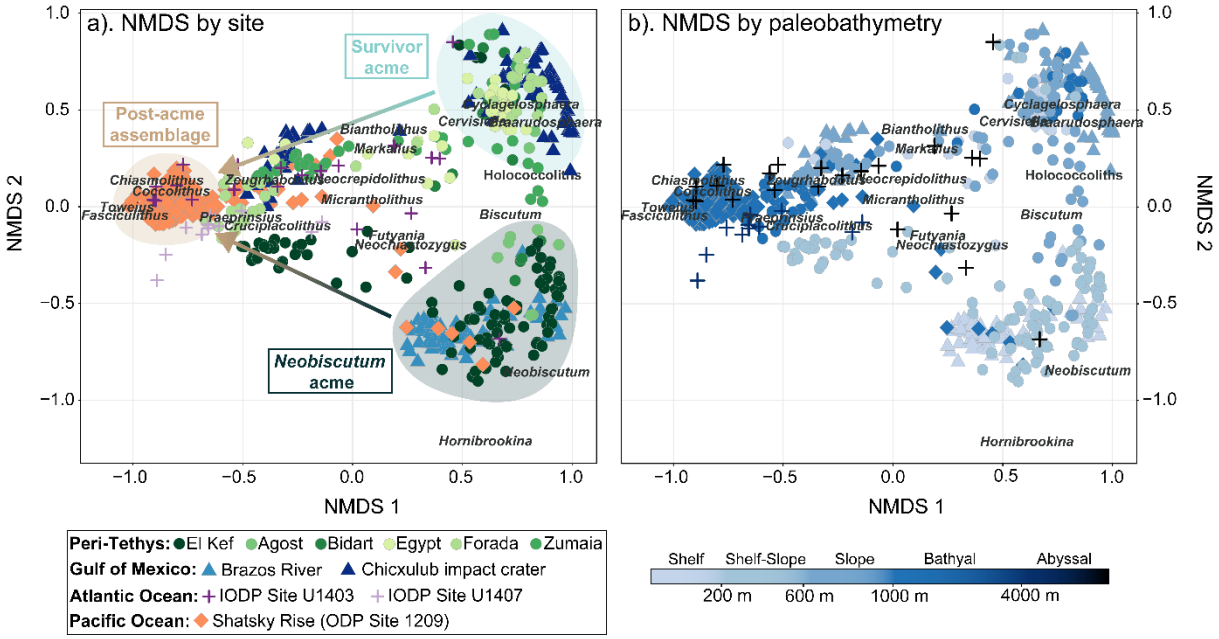

Figure 7. Nonmetric multidimensional scaling (NMDS) ordination plot for the global literature data. (a) Sample scores coded by region (shape) and site (color). Sites from the peri Tethys Ocean (circles) are El Kef (this study), Agost (Jiang et al. 2010), Bidart (Jiang et al. 2019), Egypt (Wadi Hamama & Gebel Qrieya; Tantawy 2003), Forada (Fornaciari et al. 2007) and Zumaia (Jiang et al. 2019). Sites from the Gulf of Mexico (triangles) are Brazos River (Schueth 2009) and IODP-ICDP Site M0077A: Chicxulub impact crater (Jones et al. 2019). Sites from the North Atlantic Ocean (crosses) are IODP Site U1403 and IODP Site U1407 (Bown et al. 2023). Site from the North Pacific Ocean (diamonds) is ODP Site 1209: Shatsky Rise (Alvarez et al. 2019). (b) Sample scores coded by paleobathymetry.

Paleocene assemblages. In contrast, at El Kef, the *Neobiscutum* acme is succeeded by the *Futyania* acme (which is also characterized by an increased abundance of *Cruciplacolithus*), whilst assemblages at Brazos River remain within the *Neobiscutum* acme for the entire examined time interval.

4. Discussion

4.1 Calcareous nannoplankton recovery dynamics at El Kef

The raw nannofossil relative abundance data (Figure 3a) and NMDS results (Figure 4) reveal the existence of four distinct generic acmes at El Kef, with the switchovers between them marking major milestones in the nannoplankton recovery. Below we discuss the nannofossil assemblage data and geochemical records for each of these acmes in turn, providing clues as to the potential paleoenvironmental and/or paleoecological conditions during each recovery stage.

4.1.1 Stage 1 – The Cervisiella acme (0 - 11.5 kyr post K/Pg; ~66.00 to 66.01 Ma): The oldest five samples examined in the El Kef cores – which represent the first ~11.5 kyr of the Danian – contain only *Cervisiella* calcispheres (calcareous cysts produced by dinoflagellates) and reworked Late Cretaceous nannofossil species such as *Watznaueria barnesiae*, *Micula* spp. and *Prediscosphaera* spp. This calcisphere "spike" is a global feature driven by the near-total extinction of calcareous nannoplankton (e.g., Lamolda et al., 2016; McLachlan & Pospelova, 2021; Romein, 1977), which opened up niche space that was subsequently filled by plankton groups less severely affected by the K/Pg impact (e.g., Sepúlveda et al., 2019). In addition to calcareous dinoflagellates, this included presumed opportunistic,

heterotrophic organic-walled dinoflagellate taxa (Vellekoop et al., 2015), cyanobacteria (Bralower et al., 2020; Schaefer et al., 2020), and other groups of non-calcareous phytoplankton (Sepúlveda et al., 2009), most of which have resting stages that allowed them to escape extreme surface ocean environmental conditions (e.g., global darkness and impact winter) that persisted for the years to decades following the bolide impact (Morgan et al., 2022). Although these environmental effects were geologically short-lived, an increasing body of evidence suggests prolonged surface ocean instability, potentially driven by: (1) pH overshoot following a transient ocean acidification event (up to ~40 kyr post-impact; Henehan et al., 2019), (2) long-term (~100 kyr) global warming due to increased atmospheric CO_2 from wildfires, soil decay and/or impacted target rock (Artemieva et al., 2017; Lyons et al., 2020; MacLeod et al., 2018, 2025; Morgan et al., 2022) and/or, (3) increased upwelling due to cooling-induced vertical mixing, leading to surface ocean nutrient enrichment (eutrophication) for up to 1000-2000 years post-impact (Brugger et al., 2016; Galeotti et al., 2004). Such environmental instability is supported by variability in bulk organic $\delta^{13}C$ values (-26.80 to -26.27 ‰; Figure 2) during the first 20 kyr of the Danian at El Kef, which could reflect fluctuations in terrestrial- vs. marine-derived organic material (Sosa-Montes de Oca et al., 2024), changes in marine productivity and/or non-calcifying phytoplankton community composition (Sepúlveda et al., 2019), or changes in the isotopic fractionation of carbon during photosynthesis due to the aforementioned increase in atmospheric CO_2. Although not possible with our current bulk organic geochemical data, future high-resolution, biomarker and compound-specific $\delta^{13}C$ records from El Kef will help determine which of these options was most likely.

In contrast to the bulk organic $\delta^{13}C$ data, bulk carbonate $\delta^{13}C$ values show a general ~0.7 ‰ decrease during the same interval. This was likely driven by the mass extinction of almost all latest Maastrichtian nannoplankton and planktic foraminifera species, which have relatively high $\delta^{13}C$ signatures compared to the calcareous dinoflagellate cysts (calcispheres) and small, non-symbiotic planktic foraminifera that replaced them (e.g., Alegret et al., 2012, 2022; Birch et al., 2016; Esmeray-Senlet et al., 2015; Sepúlveda et al., 2019). In addition, the absence of relatively dense, heavily calcified calcareous nannoplankton and planktic foraminifera taxa from earliest Danian communities – as well as the extinction of many larger organisms that produced fecal pellets – meant that organic matter was not transported from the surface ocean to the deep sea as effectively as it was during the latest Maastrichtian. This reduction in biological pump efficiency led to increased remineralization in the upper water column, driving down the $\delta^{13}C$ value of the planktic organisms that comprise the majority of bulk carbonate in deep-sea sediments (Figure 8a; Birch et al., 2016; D'Hondt et al., 1998; Henehan et al., 2019). Therefore, the decrease in bulk carbonate $\delta^{13}C$ likely represents the joint effect of the increased dominance of ^{13}C-depleted plankton taxa in surface ocean communities and reduced biological pump efficiency. However, it could also at least partially be explained by the increased abundance of non-biogenic carbonate – including diagenetic dolomite crystals – which are commonly observed in smear slides from both the El Kef sediment cores (Bralower et al., 2020) and outcrop section (Sepúlveda et al., 2019).

4.1.2 Stage 2 – The *Neobiscutum* acme (11.5 kyr – 1.9 Myr post K/Pg; ~64.10 to 66.00 Ma): Approximately 11.5 kyr after the mass extinction event, the earliest Danian disaster assemblages at El Kef were replaced by the *Neobiscutum* acme. This tiny, lightly calcified genus produced coccoliths <2 µm in length and likely evolved immediately after the K/Pg impact (Bown, 2005; Bown et al., 2023; Jiang et al., 2019) or during the latest Maastrichtian (Mai et al., 2003; Schueth et al., 2015). *Neobiscutum* is morphologically similar to the dominant nannoplankton species in the modern ocean

– *Gephyrocapsa* (formerly *Emiliania*) *huxleyi* – and is widely considered to have been an opportunistic, generalist taxon that was able to take advantage of high nutrient (eutrophic) surface ocean environments (e.g., Bown, 2005; Jiang et al., 2010; Jiang et al., 2019). Such conditions likely prevailed at El Kef due to reduced biological pump efficiency and increased remineralization within the ocean mixed layer, explaining the exceptionally high dominance of *Neobiscutum* (60-95% of assemblages) at this continental shelf/outer ramp site (Figures 3a; 6; 7).

Approximately 172 kyr post-impact (~65.85 Ma), there was an increase in the relative abundance of both calcispheres and *Braarudosphaera* (Figure 3a), the latter of which reached a maximum of 20% at 65.81 Ma. Interestingly, this paleoecological shift roughly coincides with a transient ~1 ‰ decrease in bulk carbonate $\delta^{18}O$ between ca. 65.90 and 65.82 Ma (Figure 3b), suggesting a brief interval of surface ocean warming. Although the bulk carbonate $\delta^{18}O$ record should be interpreted with caution due to its low signal to noise ratio and potential diagenetic imprint (e.g., Sepúlveda et al., 2019), changes in other geochemical parameters are also apparent including: (1) a ~2 ‰ decrease in bulk carbonate $\delta^{13}C$ between 65.93 and 65.86 Ma (Figure 3b) followed by a return to pre-excursion values between 65.86 and 65.82 Ma, (2) a decrease in carbonate content from 40 to 10 wt. % between 65.94 and 65.84 Ma (Figure 3d) and, (3) a ~0.5% decrease in wt. % TOC between 65.90 and 65.82 Ma (Figure 3d). These geochemical signatures closely resemble those of the astronomically-paced Dan-C2 hyperthermal

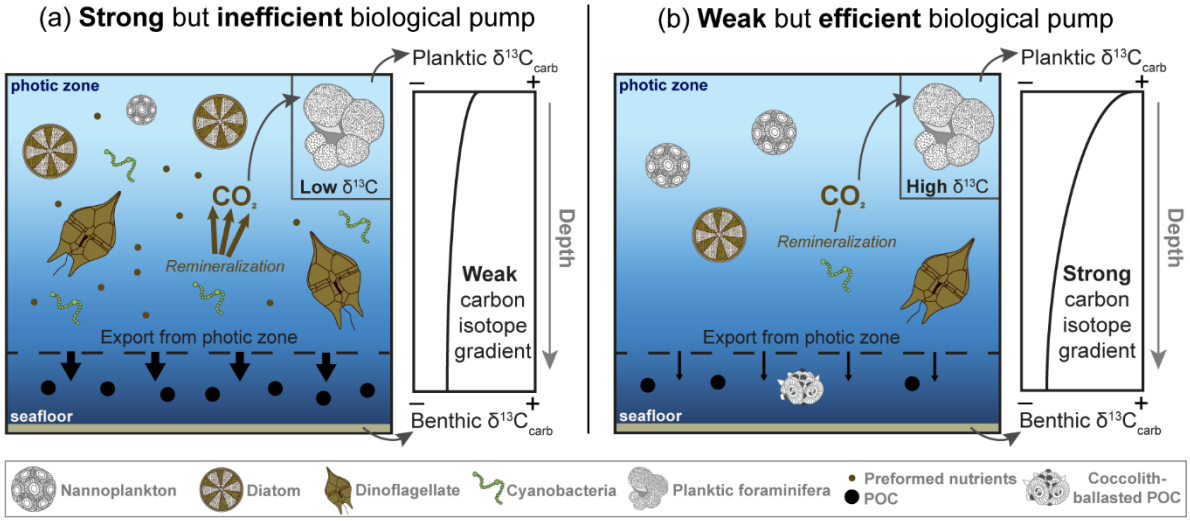

Figure 8. Conceptual model of (a) a strong but inefficient versus (b) a weak but efficient biological pump in the context of this study. (a) An inefficient biological pump may occur when phytoplankton do not fully utilize all available nutrients due to other limiting growth factors such as iron availability, light limitation or grazing pressure. As a result, only a small fraction of the available nutrients is converted into organic matter during photosynthesis and exported to the deep sea. Surface waters remain nutrient-rich (eutrophic), favoring plankton groups such as cyanobacteria, dinoflagellates and opportunistic or generalist nannoplankton taxa (e.g., *Neobiscutum*), as well as those adapted to eutrophic environments (e.g., *Braarudosphaera*). Increased remineralization in the upper water column leads to reduced planktic foraminiferal $\delta^{13}C$ values and a weak planktic-benthic carbon isotope gradient. (b) In contrast, an efficient biological pump develops when nutrients are fully utilized by phytoplankton, converted into organic matter and exported to the deep sea. This process depletes surface nutrients, favoring low-nutrient (oligotrophic)-adapted groups such nannoplankton, especially 'typical' specialized taxa (e.g., *Cruciplacolithus* and *Coccolithus*). Relatively low surface ocean remineralization results in higher planktic foraminiferal $\delta^{13}C$ values and a strong carbon isotope gradient.

event, which occurred ~160 kyr after the K/Pg boundary (i.e., ca. 65.86 Ma) and has been recognized at various Atlantic and Tethyan sites (e.g., Arreguín-Rodríguez et al., 2021; Barnet et al., 2019; Coccioni et al., 2010; Quillévéré et al., 2008). Notably, at Gubbio (Italy), a *Braarudosphaera* spike is coincident with the onset of the Dan-C2 event (Coccioni et al., 2010), supporting the identification of this earliest Paleogene hyperthermal within the El Kef sediment cores. Similar to *Neobiscutum*, the extant Cretaceous survivor *Braarudosphaera* is adapted to high nutrient environments, being restricted to coastal regions in the modern ocean (e.g., Hagino et al., 2009; Takano et al., 2006). As *Neobiscutum* remains the dominant component of nannofossil assemblages during the Dan-C2 event, it is unlikely that changes in nutrient availability were the direct cause of the *Braarudosphaera* spike. Instead, we suggest that Dan-C2 warming may have led to enhanced stratification of the upper water column, leading to temporarily reduced surface water salinity: a mechanism proposed for the formation of astronomically-paced *Braarudosphaera* "blooms" in the mid-Oligocene South Atlantic Ocean (Liebrand et al., 2018).

The decreased relative abundance of *Braarudosphaera* after the Dan-C2 event marks a return to almost monospecific *Neobiscutum* assemblages, albeit with a small, sustained increase in ancestral *Praeprinsius* (cf. *vegrandis*). From 260 kyr to 1.9 Myr post-impact (~64.10 - 65.76 Ma), nannofossil assemblages remain relatively stable (Figure 3a). This interval is also associated with a gradual decline in wt. % $CaCO_3$ (following a prior sharp increase, likely driven by the increased abundance of heavily-calcified *Braarudosphaera*), a gradual ~0.75 ‰ increase in bulk organic $\delta^{13}C$ and a sharp decrease in wt. % TOC followed by a steady decrease to the top of the *Neobiscutum* acme (Figure 3c, d). In contrast, there is very little change in the bulk carbonate $\delta^{18}O$ or $\delta^{13}C$ records (Figure 3b), the latter of which fluctuates around an average value of -0.07 ‰. Although the planktic-to-benthic foraminiferal $\delta^{13}C$ gradient (Figure 8) would ideally be used to evaluate changes in biological pump efficiency during the *Neobiscutum* interval, these data are not yet available for the El Kef cores. However, a previous study at Walvis Ridge in the mid-latitude South Atlantic suggests that the increased vertical $\delta^{13}C$ gradient during the early Danian was predominantly driven by increased planktic foraminiferal $\delta^{13}C$ rather than decreased benthic foraminiferal $\delta^{13}C$ (Birch et al., 2016). Assuming that this is the case, the relatively static bulk carbonate $\delta^{13}C$ values indicates continued biological pump inefficiency at El Kef for at least 1.9 Myr post-impact, which is supported by the negative correlation between the relative abundance of *Neobiscutum* and bulk carbonate $\delta^{13}C$ (Figure 5). Biological pump inefficiency was likely driven – at least in part – by the dominance of *Neobiscutum*, which had an average cell volume an order of magnitude smaller than the subsequent, long-ranging Paleocene taxa (Alvarez et al., 2019). This would have severely reduced the effectiveness of coccolith calcite in ballasting organic matter, thus maintaining biological pump inefficiency and high-nutrient surface oceans that further bolstered the *Neobiscutum* acme. Therefore, it is likely that the restoration of biological efficiency at El Kef may have not begun properly until *Neobiscutum* was displaced.

4.1.3 Stage 3 – The *Futyania* acme (1.9 - 3.6 Myr post-impact; ~62.46 to 64.10 Ma): The switchover between the *Neobiscutum* and *Futyania* acmes occurs across the ~64.10 Ma unconformity (Figures 3a; 4a) and is associated with: (1) a ~1.5 ‰ increase in bulk carbonate $\delta^{13}C$ (Figure 3b), (2) a ~1 ‰ decrease in bulk organic $\delta^{13}C$ (Figure 3c) and, (3) a tripling of wt. % $CaCO_3$ (Figure 3d). As the duration of the unconformity is currently poorly constrained, it is not possible to ascertain how quickly this paleoecological transition occurred. However, the large changes observed in almost all of our geochemical records signal a major regime shift (Figure 4b), with ecosystem function being very different compared to that within the preceding *Neobiscutum* acme. In particular, the concurrent

increase in bulk carbonate $\delta^{13}C$ and decrease in bulk organic $\delta^{13}C$, suggests that the *Neobiscutum* → *Futyania* dominance switchover marks the first milestone in the restoration of biological pump efficiency (Figure 8). This meant that a higher proportion of the nutrients in the surface ocean were utilized by phytoplankton, converted into organic matter and exported to the deep sea, lowering mixed layer remineralization and reducing nutrient availability. Lower nutrient (meso/oligotrophic) conditions would have favored the proliferation of typical open-ocean taxa such as *Cruciplacolithus*, as supported by their increased relative abundance in line with the onset of the *Futyania* acme at El Kef (Figure 3b). Although the paleoecological preferences of *Futyania* itself are uncertain, it is likely that it was better-adapted to lower nutrient conditions than *Neobiscutum*, making it (at the very least) a mesotrophic taxon (Jones et al., 2019; Lowery et al., 2021).

The transition from nannofossil assemblages with dominant *Neobiscutum* (14 μm^3 average cell volume) to those with higher relative abundances of *Futyania* (322 μm^3 average cell volume) and *Cruciplacolithus* (155-475 μm^3 average cell volume) almost certainly contributed to the 3x increase in wt. % $CaCO_3$ that was also observed at this time (Figure 3d, Alvarez et al., 2019). This would have improved the effectiveness of coccolith calcite as organic matter ballasts (Figure 8b), further enhancing biological pump efficiency. However, as the *Neobiscutum* → *Futyania* transition occurred across an unconformity, it is uncertain whether nannofossil assemblage changes drove enhanced biological pump efficiency or vice versa. For example, a paleoenvironmental factor such as surface warming may have increased surface ocean stratification and lowered nutrient availability, driving the observed shifts in nannofossil assemblages that in turn led to increased biological pump efficiency. Conversely, a different parameter such as the faster recovery of planktic foraminifera compared to nannoplankton and/or the reemergence of larger organisms at higher trophic levels, could have led to enhanced biological pump efficiency, lowering surface ocean nutrient availability and driving the transition from eutrophic-to meso/oligotrophic-adapted nannoplankton communities. This causality conundrum highlights the need for multiproxy records that document changes in nannofossil and planktic foraminifera assemblages, the planktic to benthic foraminiferal $\delta^{13}C$ gradient, biomarker records, and temperature proxy data at a high temporal resolution.

The remainder of the *Futyania* acme is characterized by a gradual decline in *Futyania* relative to *Cruciplacolithus* (Figure 3a). *Coccolithus* became an important component of assemblages beginning at ca. 63.86 Ma (~2.2 Myr post-impact), and gradually increased in relative abundance throughout the *Futyania* acme, whilst *Praeprinsius* maintained a consistently low (~10%) relative abundance until ~62.63 Ma (~3.6 Myr post-impact). The increased proportion of pelagic taxa such as *Cruciplacolithus* and *Coccolithus* with quasi-stability in the geochemical data, suggests a gradual transition to more oligotrophic surface waters between 63.86 and 62.63 Ma (2.2 to 3.6 Myr post-impact), which may have been predominantly ecologically – rather than environmentally – driven (Figures 3-5). At ~62.63 Ma the relative abundance of *Praeprinsius* increased to comprise >50% of assemblages. For the subsequent ca. 200 kyr, there was significant ecological jostling between *Futyania* and *Praeprinsius*, with the base of the *Praeprinsius* acme tentatively placed at ~62.46 Ma (3.6 Myr post-impact), when assemblages stabilized and *Praeprinsius* maintained its dominance. This 200 kyr transitional interval coincides with a transient ~2.5 ‰ decrease in bulk carbonate $\delta^{18}O$ (Figure 3b), a gradual 1.5 ‰ increase in bulk carbonate $\delta^{13}C$ (Figure 3b), a transient ~0.75 ‰ decrease in bulk organic $\delta^{13}C$ (Figure 3c) and wildly fluctuating wt. % $CaCO_3$ values (Figure 3d). Aside from the bulk carbonate $\delta^{13}C$, these geochemical trends are similar to those during the earlier Dan-C2 event. We therefore speculate that at least some of the paleoecological instability observed in nannofossil assemblages was a result of a

further hyperthermal such as the Late Danian Event (LDE). Although our current age model suggests that this potential warming event at El Kef occurred earlier (~62.52 Ma) than the estimated age of the LDE (~62.15 Ma; Harbich et al., 2024), the duration of planktic foraminiferal zone P2 – within which this event occurs – is poorly constrained. Therefore, if this event indeed corresponds to the LDE, it could provide valuable constraints for refining the El Kef age model in future studies.

4.1.4 Stage 4 – *The Praeprinsius* acme (3.6 – 3.7 Myr post-impact; ~62.35 to 62.46 Ma): The youngest ~100 kyr of the El Kef record is characterized by the high dominance of *Praeprinsius* (generally >70%) with very low relative abundances of *Cruciplacolithus* and *Coccolithus*, especially compared to the *Futyania* acme. The decline in oligotrophic-adapted taxa and the dominance of *Praeprinsius* – a presumed opportunistic, eutrophic-adapted taxon (Jiang et al., 2019) suggests a reversion to higher nutrient surface waters. The part of the *Praeprinsius* acme recorded at El Kef, is associated with only minor changes in the geochemical proxy records suggesting relatively quiescent paleoenvironmental conditions. Overall, the persistence of high dominance, low diversity nannoplankton acmes for at least 3.7 Myr post-impact, suggests that ecosystem function was restored a lot slower at El Kef than at ODP Site 1209, where boom-bust successions ended within ~1.8 Myr (Alvarez et al., 2019).

4.2 Regional vs. bathymetric controls on post K/Pg nannoplankton community composition

The two-way cluster analysis indicates that El Kef has an exceptionally dominant *Neobiscutum* and *Futyania* acme compared to other Tethyan sites (Clusters 2 and 3B; Figure 6), most of which sample slightly deeper (~600 to 1500 m) paleo-water depths. Curiously, the Egyptian continental shelf sites Wadi Hamama and Gebel Qreiya – which are estimated to be shallower (100-200 m; Tantawy, 2003) than El Kef (200-600 m; Alegret et al., 2022) – also do not have a well-defined *Neobiscutum* or *Futyania* acme, and are instead characterized by the distinctive 'disaster' assemblages observed at all of the analyzed upper/mid-bathyal Tethyan sites (Cluster 1; Figure 6). Examination of the Northern Hemisphere NMDS results indicates that this is unusual, as the dominance of certain nannoplankton taxa is primarily driven by paleobathymetry (Figure 7b) rather than regional controls on assemblages (Figure 7a). For example, earliest Danian disaster assemblages (calcispheres, *Braarudosphaera* and Cretaceous survivors such as *Cyclagelosphaera*) were a common feature of continental slope and bathyal sites (Figure 7b) regardless of ocean basin (Figure 7a), whereas a true, long-lasting *Neobiscutum* acme was confined to only El Kef (a continental shelf/outer ramp site) and Brazos River (a continental shelf site in the Gulf of Mexico; Schueth, 2009). The high dominance of *Neobiscutum* at both other shelf/slope sites thus makes it even more unusual that this acme was not observed in the Egyptian outcrop sections.

To explore this further, we scaled the NMDS scores in Figure 7 by the relative abundance of the six acme-forming nannofossil taxa (*Braarudosphaera*, *Neobiscutum*, *Futyania*, *Praeprinsius*, *Cruciplacolithus* and *Coccolithus*) within that sample, coded by both ocean basin/region (Figure 9) and estimated paleo-water depth (Figure 10). A comparison of these two figures confirms that with the exception of *Braarudosphaera* and *Praeprinsius*, the geographic distribution of the acme-forming nannofossil taxa is predominantly driven by paleobathymetry (Figure 10). Although *Braarudosphaera* is more abundant in the Tethys Ocean and the Gulf of Mexico (Figure 9a), its acme is restricted to continental slope-to-middle bathyal paleoenvironments (~600 to 1500 m paleo-water depth), with the exception of the previously-identified shallow water Egyptian sections (Figure 10a). In contrast, as aforementioned, *Neobiscutum* only formed a sustained long-term acme at continental shelf/outer ramp sites (~100-600 m paleo-water depth; Figure 10b), with bathyal sites such as ODP Site 1209 and

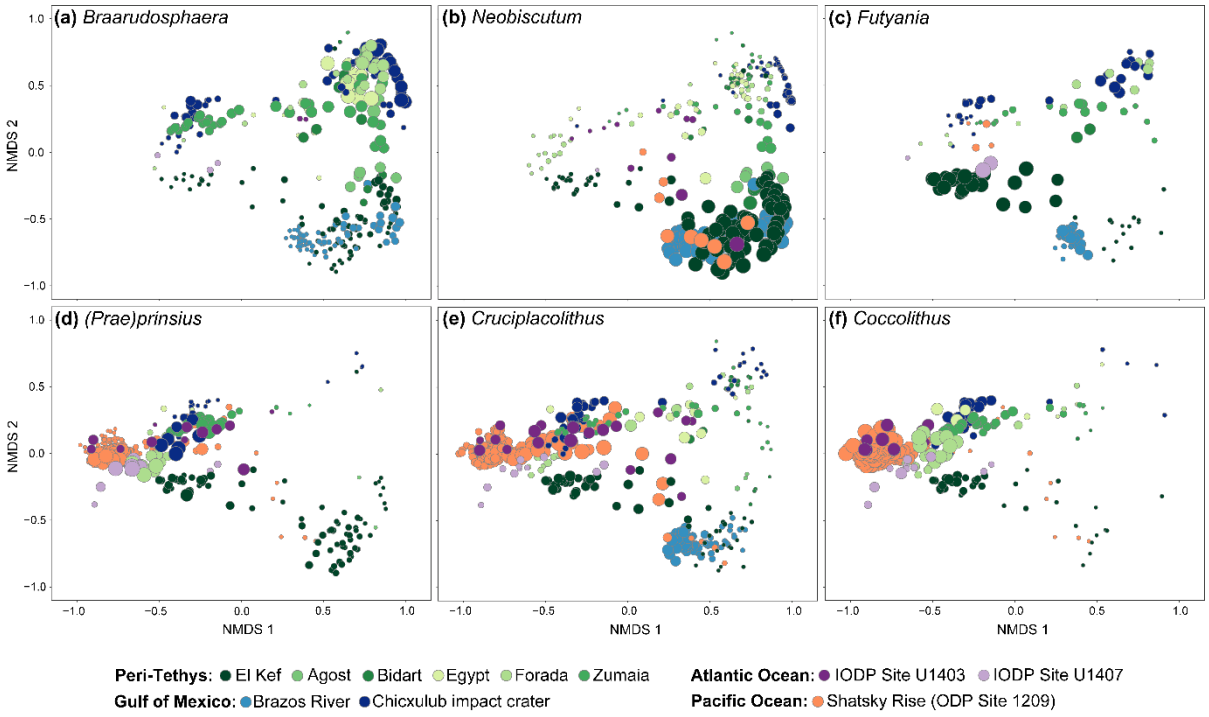

Figure 9. Nonmetric multidimensional scaling (NMDS) ordination plots showing sample scores coded by site. The size of each point (sample score) is scaled by the relative abundance of the six major acme-forming taxa: (a) *Braarudosphaera*, (b) *Neobiscutum,* (c) *Futyania,* (d) *(Prae)prinsius*, (e) *Cruciplacolithus,* (f) *Coccolithus*.

IODP Site U1403 only comprising dominant *Neobiscutum* within a limited number of samples (Figures 9b; 10b). The lower than expected relative abundance of *Neobiscutum* at Wadi Hamama and Gebel Qreiya, may therefore either be a function of the unique position of these outcrop sections in the eastern Tethys and/or their slightly more tropical paleolatitude compared to the other Tethyan sites (Figures 1; 2).

Although Tethyan ocean circulation patterns are poorly constrained for the Late Cretaceous/early Paleocene, neodymium isotopic records (Soudry et al., 2006) indicate that the strength of the westward flowing Tethyan Circumglobal Current may have increased during the latest Cretaceous due to the opening of the equatorial Atlantic gateway at the Cenomanian-Turonian boundary (Poulsen et al., 2003) and or/an enhanced latitudinal temperature gradient following Santonian cooling (Barrera & Savin, 1999). The latter mechanism would have strengthened the trade winds, leading to increased incursion of Indo-Pacific waters into the eastern Tethys and enhanced upwelling along the southeastern Tethyan continental shelf (Soudry et al., 2006), potentially explaining the observed differences in the Egyptian nannofossil assemblages compared to the other (western) Tethyan sites. Alternatively, the low-paleolatitude (~10 °N) location of Wadi Hamama and Gebel Qrieya combined with a potentially enhanced latitudinal temperature gradient, may have driven the formation of a *Braarudosphaera* acme due to stratification: the same mechanism invoked for the *Braarudosphaera* spike during the Dan-C2 event at El Kef. Although we consider the second explanation more plausible, nannofossil records from the mid-latitude eastern Tethys are required to support this hypothesis.

In comparison to all other acme-forming taxa*, Futyania* is observed at much lower overall relative abundances across all sites and only forms a true acme (>40% of assemblages) at El Kef (Figures 9; 10).

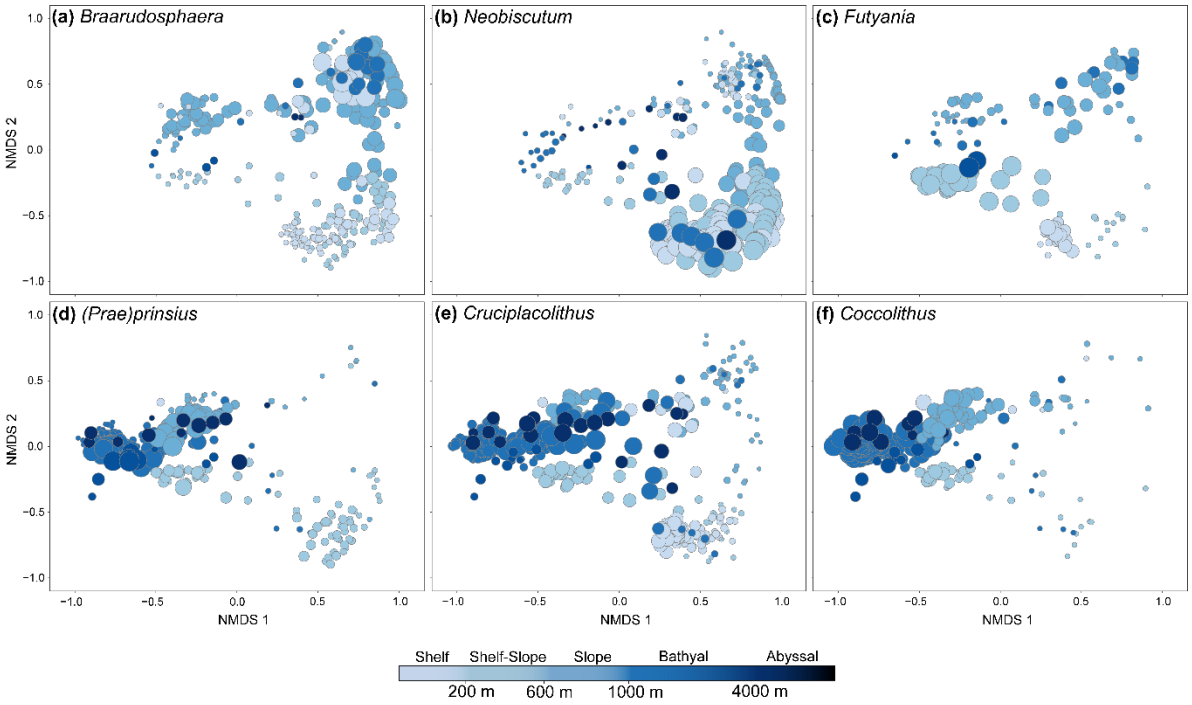

Figure 10. Nonmetric multidimensional scaling (NMDS) ordination plots showing sample scores coded by palebathymetry. The size of each point (sample score) is scaled by the relative abundance of the six major acme-forming taxa: (a) *Braarudosphaera*, (b) *Neobiscutum,* (c) *Futyania,* (d) *(Prae)prinsius*, (e) *Cruciplacolithus,* (f) *Coccolithus*.

This taxon was observed to some extent in all of the examined ocean basins, but appears to have been particularly well-adapted to continental shelf/outer ramp surface ocean environments (200-600 m paleo-water depth; Figure 10c), with Brazos River being the only other site where *Futyania* reached a sufficiently high abundance to be almost considered an acme (Figure 9c). Conversely, the *Praeprinsius* acme is a common feature of almost all sites included in the NMDS analysis during the later recovery interval (Figure 9d) regardless of paleo-water depth (Figure 10d). It is important to note that the seemingly higher abundance of *Praeprinsius* at bathyal and abyssal sites is because only samples up to the first ~3.5 Myr of the Danian were included in this analysis (with the exception of the Brazos River record, which only extends to ~2.2 Myr post-impact), to ensure that a similar time interval was being compared across all sites. However, as the *Praeprinsius* acme was not fully established until later than this at El Kef – and likely also at other shelf/slope sites – it is not visible in our Northern Hemisphere NMDS analysis.

The long-ranging Paleocene taxon *Cruciplacolithus* is present at all of the examined sites, but only forms its own acme at bathyal ODP Site 1209 (Figure 9e). At all other sites, *Cruciplacolithus* is a secondary component of one of the other acmes, such as the *Neobiscutum* acme at Brazos River, the *Futyania* acme at El Kef, and the *Praeprinsius* and/or *Coccolithus* acme at bathyal/abyssal sites in the Gulf of Mexico, peri-Tethys and North Atlantic Ocean (Figure 9e). Therefore, whilst *Cruciplacolithus* likely had a paleoecological preference for bathyal (potentially oligotrophic) environments (Jiang et al., 2010), it seems to have had a fairly broad range of environmental tolerances and a relatively cosmopolitan distribution during the early Danian. This is especially true when compared to *Coccolithus* (Figures 9f, 10f), which only forms a major acme at bathyal sites within the analyzed ~3.5 Myr post-impact interval. Overall, when considered together, it appears as though paleobathymetry

was the major driver in the abundance patterns of acme-forming nannofossil taxa during the K/Pg recovery interval, with a possible secondary regional control for *Braarudosphaera*.

4.3 Geographic heterogeneity in nannoplankton boom-bust successions and implications for the restoration of biological pump efficiency

4.3.1 Patterns in nannoplankton boom-bust successions: Although the NMDS results provide a general overview of geographic differences in early Danian nannofossil assemblages, they cannot be used to compare the durations of each acme and the timings of the switchovers between them. Therefore, in order to look at this in more detail, we produced cumulative abundance plots of the major acme-forming taxa for the eight sites with sufficiently high age control (Figure 11). In addition to El Kef, this included Forada, Italy (Fornaciari et al., 2007), Brazos River, Texas, USA (Schueth, 2009) and Chicxulub, Gulf of Mexico (Jones et al., 2019) – with ages estimated based on linear sedimentation rates between biostratigraphic tie points – and Zumaia, Spain (Jiang et al., 2019), ODP Site 1209, North Pacific (Alvarez et al., 2019) and IODP Sites U1403 and U1407, North Atlantic (Bown et al., 2023), which have their own published age models. Due to temporal limitations at some of the sites, we focused our comparison on the ~63.79 - 66.02 Ma stratigraphic interval.

The resulting plots provide further support that early Danian nannoplankton community composition was primarily a function of paleobathymetry, with sites sharing similar oceanic settings having the exact same sequence of nannoplankton acmes regardless of location (Figure 10). As revealed by the NMDS analysis, shallow continental shelf/slope sites have a particularly prominent *Neobiscutum* acme, which persists for the entire duration of the 2.2 Myr record at Brazos River (Figure 10e) and likely for a similar length of time at El Kef once the unconformity is taken into account (Figure 10a). The biggest difference between the Brazos River and El Kef records is the abundance of *Cruciplacolithus*, which begins to increase much earlier at Brazos River (~65.4 Ma) compared to at El Kef (~64.1 Ma). In contrast, the El Kef record includes ancestral *Praeprinsius* cf. *vegrandis* specimens – which were not recognized at Brazos River – and a clearly defined *Futyania* acme. However, as the Brazos River record does not extend beyond >2.2 Myr post-impact, it is possible that the apparent absence of the *Futyania* acme here is simply a function of data limitation. The *Praeprinsius* acme is similarly not observed in this restricted stratigraphic record as it occurred ~3.5 Myr after the mass extinction at El Kef. Overall, the currently available data indicates that the succession of nannoplankton acmes in shallow marine settings was *Neobiscutum* → *Futyania* → *Praeprinisius*, with boom-bust successions persisting well beyond 2.2 Myr post-impact. However, additional shelf/slope records are required to confirm these recovery patterns.

Nannofossil assemblages at the upper bathyal sites, Zumaia (peri-Tethys) and Chicxulub (Gulf of Mexico) also share very similar boom-bust characteristics (Figure 11b; f), with the calcisphere/*Braarudosphaera*/Cretaceous survivor acmes being the dominant feature of the earliest Danian recovery. *Neobiscutum* is also present – albeit at much lower abundances than at shallower sites – and *Futyania* is a similarly minor component of assemblages during the latter part of this acme. The 'disaster' acme at both upper bathyal sites is succeeded by the increased abundance of *Cruciplacolithus* and – most importantly – *Coccolithus*, which is rare in contemporaneous shelf-slope assemblages. In the Chicxulub impact crater, *Coccolithus* even formed a short-lived (~250 kyr), weakly defined acme before being replaced by *Praeprinsius*. Although present in both upper bathyal records, the *Praeprinsius* acme at Chicxulub occurred ~1 Myr later than at Zumaia, likely reflecting more severe, unstable environmental conditions at "ground zero" (Jones et al., 2019). Nevertheless, even at Chicxulub, this acme occurred ~2 Myr earlier than at El Kef, suggesting faster nannoplankton recovery

in these slightly deeper marine environments. Boom-bust successions continued until the end of both upper bathyal records (~2.2 Myr post-impact), indicating that full ecological recovery had not yet occurred. Overall, the boom-bust successions in lower slope – upper bathyal settings appear to have followed the sequence: Cretaceous survivor acme → *Coccolithus* (pseudo)acme → *Praeprinsius* acme.

The two examined middle bathyal records - Forada, Italy in the peri-Tethys (Figure 11c) and ODP Site 1209 (Shatsky Rise) in the equatorial North Pacific (Figure 11d) - display markedly different recovery patterns, likely reflecting the contrast between the more restricted peri-Tethys and the fully open-ocean setting of the Pacific. Forada most closely resembles upper bathyal sites, particularly Zumaia, for the first ~1 Myr of the Danian, as both are characterized by a survivor (rather than *Neobiscutum*) acme (Figure 10b, c, d). *Futyania* also formed a pseudo-acme ~250 kyr post-impact at both Forada (Figure 10c) and Zumaia (Figure 11b), but was very rare at Shatsky Rise (Figure 11d). In contrast, the ODP Site 1209 record is characterized by a *Neobiscutum* acme immediately following the mass extinction (Figure 11d). This acme lasted for ~250 kyr years before being replaced by the *Cruciplacolithus* acme, which was also coincident with a small spike in calcispheres (but not *Braarudosphaera*; Figure 10d). The *Coccolithus* acme developed at a similar time (700 kyr post-impact) at Forada and Shatsky Rise. However, at Shatsky Rise, the *Coccolithus* acme was interrupted by the *Praeprinsius* acme, which ended ~1.8 Myr post-impact and is interpreted as the first major milestone in nannoplankton recovery (Alvarez et al., 2019). In contrast, the *Praeprinsius* acme did not occur until 64.5 Ma at Forada and persisted until the top of the record (~63.8 Ma), closely mirroring the recovery patterns observed at Chicxulub (Figure 11f). The distinct boom-bust successions observed at these two middle bathyal sites likely reflects differences in ocean connectivity and circulation between the peri-Tethys (Forada) and the Pacific Ocean (Shatsky Rise), with the peri-Tethys representing a relatively restricted shallow sea receiving 'older' westward-flowing Indo-Pacific water via the Tethyan Circumglobal Current (Soudry et al., 2006). For this reason, we suggest two separate acme sequences for middle bathyal environments: *Neobiscutum* → *Cruciplacolithus* → *Coccolithus* → *Praeprinsius* for fully open-ocean settings such as Shatsky Rise, and Cretaceous survivor acme → *Futyania* pseudo-acme → *Coccolithus* → *Praeprinsius* for more restricted oceanic settings in the peri-Tethys.

Although the first ~500 kyr of the Danian are missing from lower bathyal IODP Site U1407 in the North Atlantic (Bown et al., 2023; Figure 11g), nannoplankton recovery patterns closely resemble those at Chicxulub (Figure 11f), with the notable exception of a very prominent *Praeprinsius* acme that began much earlier (~65.4 Ma) than at any other bathyal site. The subsequent termination of boom-bust successions and transition to stable assemblages comprising of long-ranging Paleocene taxa (e.g., *Towieus*), occurred almost synchronously at Site U1407 and Shatsky Rise, confirming that nannoplankton communities recovered more rapidly in open-ocean than in shallower marine environments. In contrast, abyssal Site U1403 (also in the North Atlantic) preserves only the first ~1.25 Myr of the Danian (Bown et al., 2023; Figure 11h). Overall, the nannoplankton recovery patterns at this site closely resemble those at Shatsky Rise, indicating relative homogeneity between the North Atlantic and North Pacific during the earliest Danian.

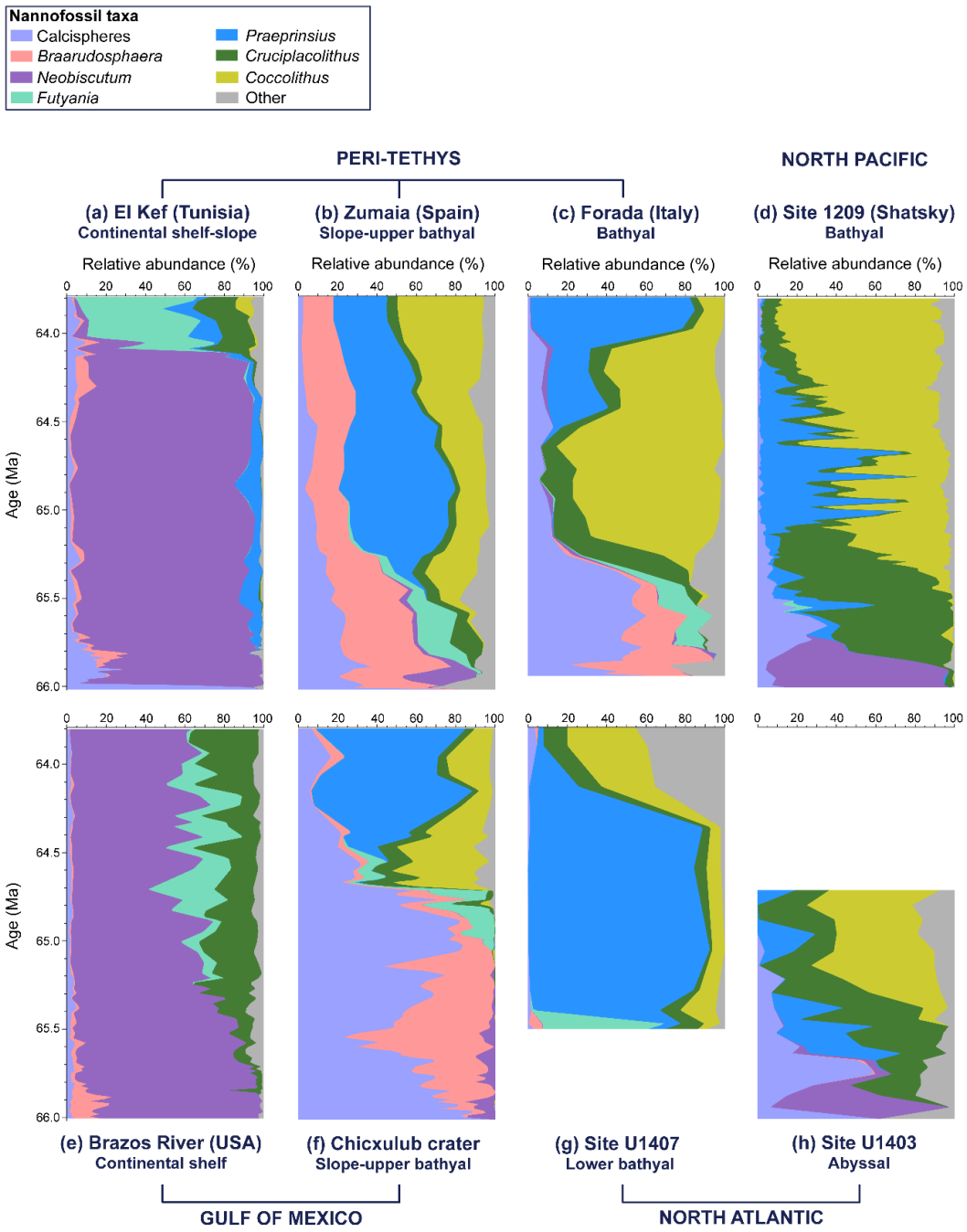

881

Figure 11. Cumulative frequency plots showing the relative abundance of the six major acme-forming nannofossil taxa (and calcispheres) between ~63.8 and 66.0 Ma at eight Northern Hemisphere sites. Please note that the traditional duration of P0 (~30 kyr) is used here to facilitate more consistent comparisons of paleoecological patterns between sites that rely on older biostratigraphic age models or employ differing age-modeling methodologies. (a) Nannofossil relative abundances at El Kef, Tunisia (this study). (b) Nannofossil relative abundances at Zumaia, Spain (Jiang et al. 2019). (c) Nannofossil relative abundances at Forada, Italy (Fornaciari et al. 2007). (d) Nannofossil relative abundances at ODP Site 1209: Shatsky Rise, North Pacific Ocean (Alvarez et al. 2019). (e) Nannofossil relative abundances at Brazos River, USA (Schueth 2009). (f) Nannofossil relative abundances at IODP-ICDP Site M0077A: Chicxulub impact crater, Gulf of Mexico (Jones et al. 2019). (g) Nannofossil relative abundances at IODP Site U1407, North Atlantic Ocean (Bown et al. 2023). (h) Nannofossil relative abundances at IODP Site U1403, North Atlantic Ocean (Bown et al. 2023).

882

4.3.2 Implications for the restoration of biological pump efficiency: The causal relationship between nannoplankton recovery and the restoration of biological pump efficiency is still open to debate, due to the various complex mechanisms that connect these two processes. For example, it remains unknown whether: (Option 1) increased nannoplankton cell volume during the early Danian enhanced the ballasting of organic matter, which drove higher biological pump efficiency, (Option 2) another mechanism independent of nannoplankton recovery (e.g. planktic foraminiferal recovery and/or the post-impact evolution of larger organisms at higher trophic levels) drove the restoration of biological pump efficiency, leading to lower nutrient surface waters that favored the proliferation of nannoplankton taxa with larger cell volumes, or (Option 3) nannoplankton recovery and the restoration of biological pump efficiency were completely decoupled. Our El Kef data provides tentative support that nannoplankton recovery and biological pump efficiency were linked – especially between the *Neobiscutum* → *Futyania* acme transition – discounting Option 3. However, it is not possible with our current data to determine whether nannoplankton recovery led (Option 1) or lagged (Option 2) the restoration of biological pump efficiency. In contrast, records from ODP Site 1209 suggest a decoupling between nannoplankton recovery and biological pump efficiency during the 'acme regime' (i.e., the first ~1.8 Myr of the Danian), although it should be noted that the ODP Site 1209 nannoplankton data were compared to the $\delta^{13}C$ gradient at ODP Site 1262 (Walvis Ridge), which were characterized by very different nannofossil assemblages (Jiang et al., 2010; Schueth et al., 2015) and export productivity patterns (Hull & Norris, 2011). Therefore, future studies should focus on comparing nannofossil abundances and geochemical reconstructions of biological pump efficiency at the same site using highly-resolved age models.

If increased nannoplankton cell volume did drive enhanced biological pump efficiency (Option 1), the distinct acme successions in shallower vs. deeper oceanic settings may at least partially explain the global heterogeneity in export productivity (Hull & Norris, 2011). For example, at shallow marine sites, the very small cell volumes that characterized the *Neobiscutum* acme (14 μm^3; Alvarez et al., 2019) dominated assemblages for at least 1.8 Myr post-impact (Figure 10), with contemporaneous bathyal sites already consisting of more diverse nannofossil assemblages with an average cell volume of ~300 μm^3 (Alvarez et al., 2019). This large disconnect between assemblage-level average cell volumes suggests – especially if Option 1 is the case – that the restoration of biological pump efficiency occurred slower-to-faster along a continental shelf-to-open ocean transect. However, as relatively rare taxa with larger cell volumes disproportionately contribute to carbonate production, this hypothesis needs to be more rigorously tested via the application of nannofossil size-trait models, which can be used to estimate changes in community-level calcite production through time (Gibbs et al., 2018; Sheward et al., 2024). The stratigraphically-expanded El Kef cores are ideal for this purpose as they contain the common coccospheres (complete nannoplankton cell coverings) required for these analyses, including intermediate morphotypes that offer the exciting opportunity to explore how traits evolved within a single species. Combining such abundance-weighted nannofossil trait data with planktic-benthic $\delta^{13}C$ records will help resolve the causal relationship between nannoplankton recovery and the restoration of biological pump efficiency during the early Danian. More broadly, our study illustrates the significance of the evolving ocean structure in shaping the recovery of nannoplankton. We suggest that changes in biological pump efficiency modulated ecological and biotic processes that drove rapidly changing boom-bust assemblages in the recovering post K-Pg ocean.

5. Conclusions

Our new El Kef nannofossil dataset – from a continental shelf/outer ramp setting in the peri-Tethys Ocean – suggests that nannoplankton boom-bust successions persisted for at least 3.7 Myr after the K/Pg mass extinction event: ~1.9 Myr longer than in the pelagic Pacific Ocean. The exact sequence of

taxa comprising nannoplankton boom-bust successions was predominantly driven by paleobathymetry (i.e., the position of a site along a continental shelf-to-open ocean transect) at both a regional (Tethyan) and global scale, whilst the timing of the switchovers between acmes had at least some regional control. We speculate that the differences in nannoplankton boom-bust successions between oceanic settings could have directly influenced the restoration of biological pump efficiency. Specifically, the earlier establishment of nannoplankton communities with a higher average cell volume (and likely enhanced ballasting potential) at open-ocean vs. continental shelf sites may have led to the faster restoration of biological pump efficiency in deeper marine environments. In the future, this should be tested directly by combining estimates for nannofossil carbonate production with reconstructions of biological pump efficiency at the same site, helping to resolve the causal relationship between these two mechanisms following the most recent mass extinction event in Earth history.

Acknowledgements

The authors would like to thank Shijun Jiang and Gilen Bernaola for providing nannofossil data from Bidart and Zumaia for our global analysis and to Heather Birch and Ursula Röhl for providing feedback on a much earlier version of this manuscript. Research funding was provided by a NASA Exobiology grant (NNX12AD83G) awarded to T.B. J.S. acknowledges support from NSF awards 2037750 and 2021648. L.K. and C.L. were supported by NSF-OCE-2037752 awarded to C.L. L.A. received funding from projects PID2023-149894OB-I00 (MCIN/AEI/10.13039/ 501100011033, FEDER, UE) and E33_23R (Gobierno de Aragón).

Conflict of interest

The authors declare no conflicts of interest relevant to this study.

Data Availability Statement

The new calcareous nannofossil relative abundance data and updated age model tables are available from PANGAEA (*doi will go here upon publication).

References

Alegret, L., Arreguín-Rodríguez, G.J. & Thomas, E. (2022). Oceanic productivity after the Cretaceous/Paleogene impact: Where do we stand? The view from the deep. In C. Koeberl, P. Claeys & A. Montanari (Eds.) *From the Guajira Desert to the Apennines, and from Mediterranean Microplates to the Mexican Killer Asteroid: Honoring the Career of Walter Alvarez: Geological Society of America Special Paper 557* (pp. 449–470). https://doi.org/10.1130/2022.2557(21)

Alegret, L., & Thomas, E. (2009). Food supply to the seafloor in the Pacific Ocean after the Cretaceous/Paleogene boundary event. *Marine Micropaleontology, 73(1-2),* 105-116. https://doi.org/10.1016/j.marmicro.2009.07.005

Alegret, L., & Thomas, E. (2013). Benthic foraminifera across the Cretaceous/Paleogene boundary in the Southern Ocean (ODP Site 690): Diversity, food and carbonate saturation. *Marine Micropaleontology, 105,* 40-51. https://doi.org/10.1016/j.marmicro.2013.10.003

Alegret, L., Thomas, E. & Lohmann, K.C. (2012). End-Cretaceous marine mass extinction not caused by productivity collapse. *Proceedings of the National Academy of Sciences*, *109(3)*, 728-732. https://doi.org/10.1073/pnas.1110601109

974 Alvarez, L.W., Alvarez, W., Asaro, F. & Michel, H.V. (1980). Extraterrestrial cause for the Cretaceous-
975 Tertiary extinction. *Science*, *208(4448)*, 1095-1108. https://doi.org/10.1126/science.208.4448.1095

976 Alvarez, S.A., Gibbs, S.J., Bown, P.R., Kim, H., Sheward, R.M. & Ridgwell, A. (2019). Diversity
977 decoupled from ecosystem function and resilience during mass extinction recovery. *Nature*, *574*,
978 242-245. https://doi.org/10.1038/s41586-019-1590-8

979 Arreguín-Rodríguez, G. J., Barnet, J. S., Leng, M. J., Littler, K., Kroon, D., Schmidt, D. N. et al. (2021).
980 Benthic foraminiferal turnover across the Dan-C2 event in the eastern South Atlantic Ocean (ODP Site
981 1262). *Palaeogeography, Palaeoclimatology, Palaeoecology, 572,* 110410.
982 https://doi.org/10.1016/j.palaeo.2021.110410

983 Artemieva, N., Morgan, J., & Expedition 364 Science Party. (2017). Quantifying the release of climate-
984 active gases by large meteorite impacts with a case study of Chicxulub. *Geophysical Research Letters,*
985 *44(20),* 10-180,188. https://doi.org/10.1002/2017GL074879

986 Barnet, J. S., Littler, K., Westerhold, T., Kroon, D., Leng, M. J., Bailey, I. et al. (2019). A high-fidelity
987 benthic stable isotope record of late Cretaceous–early Eocene climate change and carbon-cycling.
988 *Paleoceanography and Paleoclimatology, 34(4),* 672-691. https://doi.org/10.1029/2019PA003556

989 Barrera, E., & Savin, S. M. (1999). Evolution of late Campanian-Maastrichtian marine climates and
990 oceans. In E. Barrera & C.C. Johnson (Eds.), *Evolution of the Cretaceous Ocean–Climate System:*
991 *Geological Society of America Special Paper 332*, (pp. 245-282). https://doi.org/10.1130/0-8137-
992 2332-9.245

993 Birch, H.S., Coxall, H.K., Pearson, P.N., Kroon, D. & Schmidt, D.N. (2016). Partial collapse of the
994 marine carbon pump after the Cretaceous-Paleogene boundary. *Geology*, *44 (4)*, 287-290.
995 https://doi.org/10.1130/G37581.1

996 Birch, H., Schmidt, D. N., Coxall, H. K., Kroon, D., & Ridgwell, A. (2021). Ecosystem function after the
997 K/Pg extinction: decoupling of marine carbon pump and diversity. *Proceedings of the Royal Society B,*
998 *288(1953),* 20210863. https://doi.org/10.1098/rspb.2021.0863

999 Bown, P. (2005). Selective calcareous nannoplankton survivorship at the Cretaceous-Tertiary
1000 boundary. *Geology*, *33(8)*, 653-656. https://doi.org/10.1130/G21566AR.1

1001 Bown, P. R., Kim, H., & Gibbs, S. J. (2023). Danian calcareous nannofossil evolution and taxonomy
1002 with focus on sites from the North Atlantic Ocean (IODP Expedition 342, Sites U1403 and U1407).
1003 *Journal of Nannoplankton Research, 41(2),* 110-157. https://doi.org/10.58998/jnr3943

1004 Bown, P.R., Lees, J.A. & Young, J.R. (2004). Calcareous nannoplankton evolution and diversity through
1005 time. In H.R. Thierstein & J.R. Young (Eds.) *Coccolithophores* (pp. 481-508). Berlin, Heidelberg:
1006 Springer. https://doi.org/10.1007/978-3-662-06278-4_18

1007 Bown, P.R. & Young, J.R. (1998) Techniques. In P.R. Bown (Ed.), *Calcareous nannofossil*
1008 *biostratigraphy* (pp. 16-28)*.* London: Chapman and Hall.

1009 Bralower, T. J., Cosmidis, J., Heaney, P. J., Kump, L. R., Morgan, J. V., Harper, D. T. et al. (2020). Origin
1010 of a global carbonate layer deposited in the aftermath of the Cretaceous-Paleogene boundary
1011 impact. *Earth and Planetary Science Letters, 548,* 116476.
1012 https://doi.org/10.1016/j.epsl.2020.116476

1013 Brugger, J., Feulner, G., Hofmann, M., & Petri, S. (2021). A pronounced spike in ocean productivity
1014 triggered by the Chicxulub impact. *Geophysical Research Letters, 48(12),* e2020GL092260.
1015 https://doi.org/10.10

Cermeño, P. (2016). The geological story of marine diatoms and the last generation of fossil fuels. *Perspectives in Phycology, 3(2),* 53-60. https://doi.org/10.1127/pip/2016/0050

Chiarenza, A. A., Farnsworth, A., Mannion, P. D., Lunt, D. J., Valdes, P. J., Morgan, J. V., & Allison, P. A. (2020). Asteroid impact, not volcanism, caused the end-Cretaceous dinosaur extinction. *Proceedings of the National Academy of Sciences, 117(29)*, 17084-17093. https://doi.org/10.1073/pnas.2006087117

Coccioni, R., Frontalini, F., Bancalà, G., Fornaciari, E., Jovane, L., & Sprovieri, M. (2010). The Dan-C2 hyperthermal event at Gubbio (Italy): Global implications, environmental effects, and cause (s). *Earth and Planetary Science Letters, 297(1-2),* 298-305. https://doi.org/10.1016/j.epsl.2010.06.031

Coxall, H.K., D'Hondt, S. & Zachos, J.C. (2006). Pelagic evolution and environmental recovery after the Cretaceous-Paleogene mass extinction. *Geology*, *34(4)*, 297-300. https://doi.org/10.1130/G21702.1

Culver, S. J. (2003). Benthic foraminifera across the Cretaceous–Tertiary (K–T) boundary: a review. *Marine Micropaleontology, 47(3-4),* 177-226. https://doi.org/10.1016/S0377-8398(02)00117-2

D'Hondt, S., Donaghay, P., Zachos, J.C., Luttenberg, D. & Lindinger, M. (1998). Organic carbon fluxes and ecological recovery from the Cretaceous-Tertiary mass extinction. *Science*, *282(5387)*, 276-279. https://doi.org/10.1126/science.282.5387.276

Ducklow, H. W., Steinberg, D. K., & Buesseler, K. O. (2001). Upper ocean carbon export and the biological pump. *Oceanography*, *14*(4), 50-58. https://www.jstor.org/stable/43924964

Esmeray-Senlet, S., Wright, J. D., Olsson, R. K., Miller, K. G., Browning, J. V., & Quan, T. M. (2015). Evidence for reduced export productivity following the Cretaceous/Paleogene mass extinction. *Paleoceanography, 30(6),* 718-738. https://doi.org/10.1002/2014PA002724

Fornaciari, E., Giusberti, L., Luciani, V., Tateo, F., Agnini, C., Backman, J. et al. (2007). An expanded Cretaceous− Tertiary transition in a pelagic setting of the Southern Alps (central-western Tethys). *Palaeogeography, Palaeoclimatology, Palaeoecology*, *255(1-2)*, 98-131. https://doi.org/10.1016/j.palaeo.2007.02.044

Fraass, A.J., Kelly, D.C. & Peters, S.E. (2015). Macroevolutionary history of the planktic foraminifera. *Annual Review of Earth and Planetary Sciences*, *43*, 139-166. https://doi.org/10.1146/annurev-earth-060614-105059

Galeotti, S., Brinkhuis, H., & Huber, M. (2004). Records of post–Cretaceous-Tertiary boundary millennial-scale cooling from the western Tethys: A smoking gun for the impact-winter hypothesis?. *Geology, 32(6),* 529-532. https://doi.org/10.1130/G20439.1

Gibbs, S.J., Sheward, R.M., Bown, P.R., Poulton, A.J. & Alvarez, S.A. (2018). Warm plankton soup and red herrings: calcareous nannoplankton cellular communities and the Palaeocene–Eocene Thermal Maximum. *Philosophical Transactions of the Royal Society A: Mathematical, Physical and Engineering Sciences*, *376(2130),* 20170075. https://doi.org/10.1098/rsta.2017.0075.

Hagino, K., Takano, Y., & Horiguchi, T. (2009). Pseudo-cryptic speciation in *Braarudosphaera bigelowii* (Gran and Braarud) Deflandre. *Marine Micropaleontology, 72(3-4),* 210-221. https://doi.org/10.1016/j.marmicro.2009.06.001

Harbich, M., Barnet, J. S., Rae, J. W., & Kroon, D. (2024). Warming, acidification, and calcification feedback during the first hyperthermal of the Cenozoic—The Latest Danian Event. *Geology, 52(1),* 51-55. https://doi.org/10.1130/G51330.1

Harrell Jr, F.E. (2025). Hmisc: Harrell Miscellaneous. https://CRAN.R-project.org/package=Hmisc

Henehan, M.J., Ridgwell, A., Thomas, E., Zhang, S., Alegret, L., Schmidt, D.N. et al. (2019). Rapid ocean acidification and protracted Earth system recovery followed the end-Cretaceous Chicxulub impact. *Proceedings of the National Academy of Sciences*, *116(45)*, 22500-22504. https://doi.org/10.1073/pnas.1905989116

Henson, S. A., Sanders, R., Madsen, E., Morris, P. J., Le Moigne, F., & Quartly, G. D. (2011). A reduced estimate of the strength of the ocean's biological carbon pump. *Geophysical Research Letters, 38(4),* L04606, https://doi.org/10.1029/2011GL046735

Hilting, A. K., Kump, L. R., & Bralower, T. J. (2008). Variations in the oceanic vertical carbon isotope gradient and their implications for the Paleocene-Eocene biological pump. *Paleoceanography*, *23(3),* PA3222. https://doi.org/10.1029/2007PA001458

Hsü, K. J., & Mckenzie, J. A. (1985). A “Strangelove” ocean in the earliest Tertiary. In E.T. Sundquist & W.S. Broecker (Eds.), *The Carbon Cycle and Atmospheric CO_2: Natural Variations Archean to Present. Geophysical Monographs Series 32,* 487-492. https://doi.org/10.1029/GM032p0487

Hull, P. (2015). Life in the aftermath of mass extinctions. *Current Biology, 25(19),* R941-R952. https://doi.org/10.1016/j.cub.2015.08.053

Hull, P.M., Bornemann, A., Penman, D.E., Henehan, M.J., Norris, R.D., Wilson, P.A. et al. (2020). On impact and volcanism across the Cretaceous-Paleogene boundary. *Science*, *367(6475)*, 266-272. https://doi.org/10.1126/science.aay5055

Hull, P.M. & Norris, R.D. (2011). Diverse patterns of ocean export productivity change across the Cretaceous-Paleogene boundary: New insights from biogenic barium. *Paleoceanography*, *26*, PA3205. https://doi.org/10.1029/2010PA002082

Hull, P. M., Norris, R. D., Bralower, T. J., & Schueth, J. D. (2011). A role for chance in marine recovery from the end-Cretaceous extinction. *Nature Geoscience, 4(12),* 856-860. https://doi.org/10.1038/ngeo1302

Jiang, S., Bralower, T.J., Patzkowsky, M.E., Kump, L.R. & Schueth, J.D. (2010). Geographic controls on nannoplankton extinction across the Cretaceous/Palaeogene boundary. *Nature Geoscience*, *3*, 280-285. https://doi.org/10.1038/ngeo775

Jiang, S., Chen, X., & Bernaola, G. (2019). Environmental controls on calcareous nannoplankton response to the Cretaceous/Paleogene mass extinction in the Tethys realm. *Palaeogeography, Palaeoclimatology, Palaeoecology, 515,* 134-142. https://doi.org/10.1016/j.palaeo.2017.12.044

Jones, H.L., Lowery, C.M. & Bralower, T.J. (2019). Delayed calcareous nannoplankton boom-bust successions in the earliest Paleocene Chicxulub (Mexico) impact crater. *Geology*, *47(8)*, 753-756. https://doi.org/10.1130/G46143.1

Jones, H. L., Westerhold, T., Birch, H., Hull, P., Negra, M. H., Röhl, U. et al. (2023). Stratigraphy of the Cretaceous/Paleogene (K/Pg) boundary at the Global Stratotype Section and Point (GSSP) in El Kef, Tunisia: New insights from the El Kef Coring Project. *GSA Bulletin, 135(9-10),* 2451-2477. https://doi.org/10.1130/B36487.1

Junium, C. K., Zerkle, A. L., Witts, J. D., Ivany, L. C., Yancey, T. E., Liu, C., & Claire, M. W. (2022). Massive perturbations to atmospheric sulfur in the aftermath of the Chicxulub impact. *Proceedings of the National Academy of Sciences, 119(14),* e2119194119. https://doi.org/10.1073/pnas.2119194119

Kolde, R. (2025). pheatmap: Pretty Heatmaps. https://CRAN.R-project.org/package=pheatmap

Knoll, A.H. & Follows, M.J. (2016). A bottom-up perspective on ecosystem change in Mesozoic oceans. *Proceedings of the Royal Society B: Biological Sciences*, *283(1841)*, 20161755. https://doi.org/10.1098/rspb.2016.1755

Lamolda, M. A., Melinte-Dobrinescu, M. C., & Kaiho, K. (2016). Calcareous nannoplankton assemblage changes linked to paleoenvironmental deterioration and recovery across the Cretaceous–Paleogene boundary in the Betic Cordillera (Agost, Spain). *Palaeogeography, Palaeoclimatology, Palaeoecology, 441,* 438-452. https://doi.org/10.1016/j.palaeo.2015.10.003

Liebrand, D., Raffi, I., Fraguas, Á., Laxenaire, R., Bosmans, J.H., Hilgen, F.J. et al. (2018). Orbitally Forced Hyperstratification of the Oligocene South Atlantic Ocean. *Paleoceanography and Paleoclimatology*, *33*, 511-529. https://doi.org/10.1002/2017PA003222

Lowery, C.M., Bown, P.R., Fraass, A.J. & Hull, P.M. (2020). Ecological Response of Plankton to Environmental Change: Thresholds for Extinction. *Annual Review of Earth and Planetary Sciences*, *48*, 403-429. https://doi.org/10.1146/annurev-earth-081619-052818

Lowery, C. M., Jones, H. L., Bralower, T. J., Cruz, L. P., Gebhardt, C., Whalen, M. T. et al. (2021). Early Paleocene paleoceanography and export productivity in the Chicxulub crater. *Paleoceanography and Paleoclimatology, 36(11),* e2021PA004241. https://doi.org/10.1029/2021PA004241

Lyons, S. L., Karp, A. T., Bralower, T. J., Grice, K., Schaefer, B., Gulick, S. P. et al. (2020). Organic matter from the Chicxulub crater exacerbated the K–Pg impact winter. *Proceedings of the National Academy of Sciences*, *117(41),* 25327-25334. https://doi.org/10.1073/pnas.2004596117

MacLeod, K. G., Huber, B. T., Tabor, C., Mitra, S., Wheatley, R., Harrison, C. et al. (2025). Isotopic evidence from a Brazos River (Texas, USA) Cretaceous/Paleogene boundary section consistent with a pulse of greenhouse warming shortly after the Chicxulub impact. *Global and Planetary Change, 253,* 104924. https://doi.org/10.1016/j.gloplacha.2025.104924

MacLeod, K. G., Quinton, P. C., Sepúlveda, J., & Negra, M. H. (2018). Postimpact earliest Paleogene warming shown by fish debris oxygen isotopes (El Kef, Tunisia). *Science*, *360*(6396), 1467-1469. https://doi.org/10.1126/science.aap8525

MacRae, R. A., Fensome, R. A., & Williams, G. L. (1996). Fossil dinoflagellate diversity, originations, and extinctions and their significance. *Canadian Journal of Botany, 74(11),* 1687-1694. https://doi.org/10.1139/b96-205

Mai, H., Speijer, R.P. & Schulte, P. (2003). Calcareous index nannofossils (coccoliths) of the lowermost Paleocene originated in the late Maastrichtian. *Micropaleontology*, *49(2)*, 189-195. https://doi.org/10.2113/49.2.189

Mather, B. R., Müller, R. D., Zahirovic, S., Cannon, J., Chin, M., Ilano, L. et al. (2024). Deep time spatio-temporal data analysis using pyGPlates with PlateTectonicTools and GPlately. *Geoscience Data Journal, 11(1),* 3-10. https://doi.org/10.1002/gdj3.185

McLachlan, S. M., & Pospelova, V. (2021). Calcareous dinoflagellate cyst distribution across the K/Pg boundary at DSDP site 577, Shatsky Rise, western North Pacific Ocean. *Marine Micropaleontology, 168,* 102057. https://doi.org/10.1016/j.marmicro.2021.102057

Molina, E., Arenillas, I., & Arz, J. A. (1998). Mass extinction in planktic foraminifera at the Cretaceous/Tertiary boundary in subtropical and temperate latitudes. *Bulletin de la Société géologique de France, 169(3),* 351-363.

Morgan, J. V., Bralower, T. J., Brugger, J., & Wünnemann, K. (2022). The Chicxulub impact and its environmental consequences. *Nature Reviews Earth & Environment, 3(5),* 338-354. https://doi.org/10.1038/s43017-022-00283-y

Müller, R. D., Flament, N., Cannon, J., Tetley, M. G., Williams, S. E., Cao, X. et al. (2022). A tectonic-rules-based mantle reference frame since 1 billion years ago – implications for supercontinent cycles and plate–mantle system evolution [Data set]. In Solid Earth (1.2.4, Vol. 13, pp. 1127–1159). Zenodo. https://doi.org/10.5281/zenodo.13636799

Oksanen, J., Simpson, G.L., Guillaume Blanchet, F., Kindt, R., Legendre, P., Minchin, P.R. et al. (2025). vegan: Community Ecology Package, version 2.7-2. https://CRAN.R-project.org/package=vegan

Perch-Nielsen, K., McKenzie, J. & He, Q. (1982). Biostratigraphy and isotope stratigraphy and the 'catastrophic' extinction of calcareous nannoplankton at the Cretaceous/Tertiary boundary. In L.T. Silver & P.H. Schultz (Eds.), *Geological Implications of Impacts of Large Asteroids and Comets on the Earth: Geological Society of America Special Paper 190* (pp. 353-371). https://doi.org/10.1130/SPE190-p353

Philip, J. & Floquet, M. (2000). Late Maastrichtian (69.5–65 Ma). In: Crasquin, S. (Ed*.), Atlas Peri-Tethys, Paleogeographic Maps. Explanatory notes* (pp. 145-152). Paris: CCGM/CGMW.

Poulsen, C. J., Gendaszek, A. S., & Jacob, R. L. (2003). Did the rifting of the Atlantic Ocean cause the Cretaceous thermal maximum? *Geology, 31(2),* 115-118. https://doi.org/10.1130/0091-7613(2003)031<0115:DTROTA>2.0.CO;2

Quillévéré, F., Norris, R. D., Kroon, D., & Wilson, P. A. (2008). Transient ocean warming and shifts in carbon reservoirs during the early Danian. *Earth and Planetary Science Letters*, *265(3-4),* 600-615. https://doi.org/10.1016/j.epsl.2007.10.040

R Core Team. (2025, December 04). R: A Language and Environment for Statistical Computing (Version 4.5.1) [Software]. R Foundation for Statistical Computing, Vienna, Austria. https://www.R-project.org/.

Renaudie, J., Drews, E. L., & Böhne, S. (2018). The Paleocene record of marine diatoms in deep-sea sediments. *Fossil Record, 21(2),* 183-205. https://doi.org/10.5194/fr-21-183-2018, 2018.

Romein, A. J. T. (1977). Calcareous nannofossils from the Cretaceous/Tertiary boundary interval in the Barranco del Gredero (Caravaca, Prov. Murcia, SE Spain). *Proceedings of the Koninklijke Nederlandse Akademie ven Wetenschappen Amsterdam Ser. B, 80,* 256-279.

Schaefer, B., Grice, K., Coolen, M. J., Summons, R. E., Cui, X., Bauersachs, T. et al. (2020). Microbial life in the nascent Chicxulub crater. *Geology, 48(4),* 328-332. https://doi.org/10.1130/G46799.1

Schneider, L. J., Bralower, T. J., Kump, L. R., & Patzkowsky, M. E. (2013). Calcareous nannoplankton ecology and community change across the Paleocene-Eocene Thermal Maximum. *Paleobiology, 39(4),* 628-647. https://doi.org/10.1666/12050

Schueth, J.D. (2009). A Multivariate Analysis of the Recovery of Calcareous Nannoplankton and Planktonic Foraminifera from the Cretaceous/Paleogene (K/P) Mass Extinction. (Master's thesis). Retrieved from (https://etda.libraries.psu.edu/catalog/10281). University Park, PA: Penn State University.

Schueth, J.D., Bralower, T.J., Jiang, S. & Patzkowsky, M.E. (2015). The role of regional survivor incumbency in the evolutionary recovery of calcareous nannoplankton from the

Cretaceous/Paleogene (K/Pg) mass extinction. *Paleobiology*, *41(4)*, 661-679. https://doi.org/10.1017/pab.2015.28

Schulte, P., Alegret, L., Arenillas, I., Arz, J.A., Barton, P.J., Bown, P.R. et al. (2010). The Chicxulub asteroid impact and mass extinction at the Cretaceous-Paleogene boundary. *Science*, *327(5970)*, 1214-1218. https://doi.org/10.1126/science.1177265

Senel, C. B., Kaskes, P., Temel, O., Vellekoop, J., Goderis, S., DePalma, R. et al. (2023). Chicxulub impact winter sustained by fine silicate dust. *Nature Geoscience, 16(11),* 1033-1040. https://doi.org/10.1038/s41561-023-01290-4

Sepúlveda, J., Alegret, L., Thomas, E., Haddad, E., Cao, C. & Summons, R.E. (2019). Stable Isotope Constraints on Marine Productivity Across the Cretaceous-Paleogene Mass Extinction. *Paleoceanography and Paleoclimatology*, *34*, 1195-1217. https://doi.org/10.1029/2018PA003442

Sepúlveda, J., Wendler, J. E., Summons, R. E., & Hinrichs, K. U. (2009). Rapid resurgence of marine productivity after the Cretaceous-Paleogene mass extinction. *Science, 326(5949),* 129-132. https://doi.org/10.1126/science.1176233

Sheward, R. M., Herrle, J. O., Fuchs, J., Gibbs, S. J., Bown, P. R., & Eibes, P. M. (2024). Biogeochemical traits of a high latitude South Pacific Ocean calcareous nannoplankton community during the Oligocene. *Paleoceanography and Paleoclimatology, 39(12),* e2024PA004946. https://doi.org/10.1029/2024PA004946

Sims, P. A., Mann, D. G., & Medlin, L. K. (2006). Evolution of the diatoms: insights from fossil, biological and molecular data. *Phycologia, 45(4),* 361-402. https://doi.org/10.2216/05-22.1

Sosa-Montes de Oca, C., Witts, J. D., Lowery, C. M., Kearns, L. E., Garb, M. P., Naujokaityte, J. et al. (2024). Intense changes in the main source of organic carbon to the Gulf Coastal Plain following the Cretaceous-Paleogene boundary. *Paleoceanography and Paleoclimatology*, *39(8),* e2024PA004887. https://doi.org/10.1029/2024PA004887

Soudry, D., Glenn, C.R., Nathan, Y., Segal, I. & VonderHaar, D. (2006). Evolution of Tethyan phosphogenesis along the northern edges of the Arabian–African shield during the Cretaceous–Eocene as deduced from temporal variations of Ca and Nd isotopes and rates of P accumulation. *Earth-Science Reviews*, *78(1-2),* 27-57. https://doi.org/10.1016/j.earscirev.2006.03.005

Takano, Y., Hagino, K., Tanaka, Y., Horiguchi, T., & Okada, H. (2006). Phylogenetic affinities of an enigmatic nannoplankton, *Braarudosphaera bigelowii* based on the SSU rDNA sequences. *Marine Micropaleontology, 60(2),* 145-156. https://doi.org/10.1016/j.marmicro.2006.04.002

Tantawy, A.A.A.M. (2003). Calcareous nannofossil biostratigraphy and paleoecology of the Cretaceous–Tertiary transition in the central eastern desert of Egypt. *Marine Micropaleontology*, *47(3-4)*, 323-356. https://doi.org/10.1016/S0377-8398(02)00135-4

Thierstein, H. R. (1982). Terminal Cretaceous plankton extinctions: A critical assessment. In L.T. Silver & P.H. Schultz (Eds.), *Geological Implications of Impacts of Large Asteroids and Comets on the Earth: Geological Society of America Special Paper 190* (pp. 385-399). https://doi.org/10.1130/SPE190-p385

Thomas, E. (1990). Late Cretaceous-early Eocene mass extinctions in the deep sea. In V.L. Sharpton & P.D. Ward (Eds.), *Global catastrophes in Earth history; An interdisciplinary conference on impacts, volcanism, and mass mortality: Geological Society of America Special Paper 247* (pp. 481-495). https://doi.org/10.1130/SPE247-p481

Vellekoop, J., Sluijs, A., Smit, J., Schouten, S., Weijers, J.W., Damsté, J.S.S. & Brinkhuis, H. (2014). Rapid short-term cooling following the Chicxulub impact at the Cretaceous–Paleogene boundary. *Proceedings of the National Academy of Sciences*, *111(21)*, 7537-7541. https://doi.org/10.1073/pnas.1319253111

Vellekoop, J., Smit, J., van de Schootbrugge, B., Weijers, J.W., Galeotti, S., Damste, J.S.S. & Brinkhuis, H. (2015). Palynological evidence for prolonged cooling along the Tunisian continental shelf following the K–Pg boundary impact. *Palaeogeography, Palaeoclimatology, Palaeoecology*, *426,* 216-228. https://doi.org/10.1016/j.palaeo.2015.03.021

Vellekoop, J., Woelders, L., Açikalin, S., Smit, J., Van De Schootbrugge, B., Yilmaz, I.O. et al. (2017). Ecological response to collapse of the biological pump following the mass extinction at the Cretaceous-Paleogene boundary. *Biogeosciences*, *14*, 885-900. https://doi.org/10.5194/bg-14-885-2017

Wade, B. S., Pearson, P. N., Berggren, W. A., & Pälike, H. (2011). Review and revision of Cenozoic tropical planktonic foraminiferal biostratigraphy and calibration to the geomagnetic polarity and astronomical time scale. *Earth-Science Reviews, 104(1-3),* 111-142. https://doi.org/10.1016/j.earscirev.2010.09.003

Wei, T. & Simko, V. (2024). R package 'corrplot': Visualization of a Correlation Matrix (Version 0.95). https://github.com/taiyun/corrplot.

Westerhold, T., Marwan, N., Drury, A. J., Liebrand, D., Agnini, C., Anagnostou, E. et al. (2020). An astronomically dated record of Earth's climate and its predictability over the last 66 million years. *Science, 369(6509),* 1383-1387. https://doi.org/10.1126/science.aba6853

Wickham, H. (2016). ggplot2: Elegant Graphics for Data Analysis. New York: Springer-Verlag. https://ggplot2.tidyverse.org